Politecnico di Milano

SCUOLA DI INGEGNERIA INDUSTRIALE E DELL'INFORMAZIONE
Corso di Laurea Magistrale in Ingegneria Biomedica e Ingegneria Meccanica

Tesi di Laurea Magistrale

Study of an auxetic cardiac patch capable of conducting electrical signals while minimizing the impact on the mechanical functionality of an infarcted ventricle

Relatori
Prof. Jose Felix Rodriguez Matas
Prof. Stefano Foletti

Correlatori
Ing. Francesca Berti
Ing. Ludovica Cestariolo
Ing. Matteo Gavazzoni

Candidati
Nisida Masullo
Matr. 945139

Veronica Luppini
Matr. 945313

Anno Accademico 2022 – 2023

Nisida Masullo, Veronica Luppini: *Study of an auxetic cardiac patch capable of conducting electrical signals while minimizing the impact on the mechanical functionality of an infarcted ventricle* | Tesi di Laurea Magistrale in Ingegneria Biomedica e Ingegneria Meccanica, Politecnico di Milano.
© Copyright Ottobre 2023.

Politecnico di Milano:
www.polimi.it

Scuola di Ingegneria Industriale e dell'Informazione:
www.ingindinf.polimi.it

Contents

Abstract **vii**

1 Clinical context **1**
1.1 Heart morphology 1
1.2 Mechanics of heart contraction 5
1.3 Electrical conduction in the heart tissue 7
1.4 Myocardial infarction: complications and treatments . . . 12
1.5 State of the art on cardiac patches 15
1.6 Objective of the thesis 18

2 Patch geometry definition **21**
2.1 Optimization tool 21
2.2 Results 27
2.3 Discussion 35

3 Morphological characterisation of the left ventricle from clinical images **37**
3.1 Digital processing of clinical images 37
3.2 Post processing of left ventricle model 40

4 Cardiac cycle simulation with pressurization tests **43**
4.1 Tests on parallelepiped 43
4.2 Tests on semi-ellipsoid 52
4.3 Tests on realistic left ventricle 58

5 Simulation of the electrophysiology of the heart **65**
5.1 Creation of the input files 66
5.2 Simulations on simplified model 68
5.3 Simulations on heart model 73
5.4 Simulations with auxetic patch 83

6 Conclusions 87

Acknowledgements 93

List of Figures 95

List of Tables 99

Bibliography 101

Abstract

In Italy, approximately 16% of mortality is attributed to ischemic heart disease. Myocardial ischemia arises from insufficient oxygen supply, causing cell damage and impacting on both ventricular mechanics and myocardial cell electrical properties. At present, no curative devices are available to treat myocardial infarction, except for a limited number of approaches focused on repairing damaged cardiac or vascular tissue without establishing electrical integration with the tissue. A promising area of research involves myocardial tissue engineering, using hydrogels, scaffolds, and patches to support damaged tissue through cellular and non-cellular approaches. For the latter, it's crucial to restore the electrical properties while maintaining normal heart function. As a result, the mechanical properties of the patch should closely match those of heart tissue. The objective of this thesis is to study the design of an auxetic cardiac patch capable of conducting electrical signals while minimizing the impact on the mechanical functionality of an infarcted ventricle, addressing first the mechanical aspect, then the electrophysiological one. The first step explores the feasibility of utilizing an optimization tool to obtain the desired mechanical properties in an auxetic patch. The employed code proved suitable for this purpose. The mechanical simulations assessed how a patch affects ventricle deformation throughout the cardiac cycle. The findings indicate that applying a patch does not significantly alter the strain field already affected by the infarct. The electrophysiological study evaluated the patch conductivity. The outcomes confirm the capability of the device to conduct electrical signals while preserving the essential characteristics of the stimulus. This work marks an initial phase in developing a therapeutic patch and does not permit a cost-benefit analysis at this point. Nonetheless, it serves as a foundation for future and more comprehensive research on the topic.

Keywords: myocardial ischemia, optimization tool, auxetic patch, heart tissue strain field, electrical signal conduction

Chapter 1

Clinical context

1.1 Heart morphology

The heart has a predominantly muscular constitution (i.e., myocardium) and has rhythmic, autonomous contractions (on average 60-70 beats per minute in the subject at rest) that ensure blood circulation in the vessels (Figure 1.1). Each beat corresponds to a contraction phase (i.e., systole) and a relaxation phase (i.e., diastole). Inside it presents four cavities: two posterior-superior, the atria, and two antero-inferior, the ventricles, right and left respectively [2].

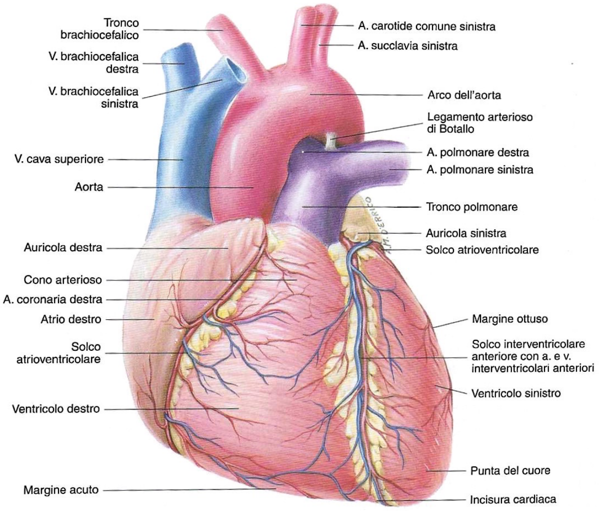
Tronco brachiocefalico
V. brachiocefalica destra
V. brachiocefalica sinistra
V. cava superiore
Aorta
Auricola destra
Cono arterioso
A. coronaria destra
Atrio destro
Solco atrioventricolare
Ventricolo destro
Margine acuto
A. carotide comune sinistra
A. succlavia sinistra
Arco dell'aorta
Legamento arterioso di Botallo
A. polmonare destra
A. polmonare sinistra
Tronco polmonare
Auricola sinistra
Solco atrioventricolare
Margine ottuso
Solco interventricolare anteriore con a. e v. interventricolari anteriori
Ventricolo sinistro
Punta del cuore
Incisura cardiaca
A.M. D'ERRICO

Figure 1.1: Heart morphology [2].

1.1.1 Structure

The heart consists of three layers that run from the surface to the inside and are: the epicardium, the myocardium, and the endocardium.

The epicardium covers the entire outer surface of the heart, making it smooth and translucent. On the surface, the epicardium consists of a mesothelium covered by a liquid veil and provided with a thin lamina propria rich in elastic fibres. It is deeply connected to the myocardium by a connective layer, the subepicardial layer, which is in direct connection with the interstitial connective tissue of the musculature. In the subepicardial layer run the main branches of the coronary vessels, which are often partially surrounded by fat deposits that are visible on the surface of the heart as yellowish spots.

The myocardium represents the thickest layer of the heart wall and is made up of a particular variety of striated muscle tissue, the myocardial tissue. Two types of myocardium can be distinguished: the common myocardium, which accounts for about 90% of all myocardium, and constitutes the cardiac musculature, both atrial and ventricular, ensuring the contractile activity of the heart, and the specific myocardium, which constitutes the conduction system specialised in performing pacemaker and contractile impulse transmission functions.

The common myocardium is made up of mononucleated elements (i.e., cardiomyocytes), with a cylindrical shape, a length of 80-100 μm and a thickness of 10-20 μm. The ends of the cardiomyocytes are divided into two or more branches that take close relationship with the ramifications of the adjacent elements by means of the intercalary discs.

The specific myocardium constitutes the conduction system and therefore the cellular elements that make it up are more oriented towards a stimulus-transmitting function rather than a contractile function. Three types of elements belonging to the specific myocardium can be distinguished: nodal cells, transition cells and Purkinje cells. Nodal cells (i.e., P cells) are concentrated in the sinoatrial and atrioventricular nodes. Transition cells are located especially at the periphery of the sinoatrial and atrioventricular nodes. Purkinje cells, also present in the division branches of the atrioventricular bundle, form the subendocardial networks in the ventricular walls.

The endocardium is a whitish, smooth, shiny membrane that covers the cardiac cavities, adapting to all the irregularities of their surface. Its thickness varies from 20 to 500 μm, reaching its maximum in the left atrium. The subendocardial layer contains the terminal branches of the heart conduction system with Purkinje cells (i.e., subendocardial networks) [2].

1.1.2 Cardiac muscles

The muscular component of the heart, consisting of myocardial tissue (i.e., common myocardium) is more developed in the ventricles (especially the left) than in the atria. Myocardial fibers (i.e., cardiomyocytes) tend to gather in bundles of varying size. The atrial and ventricular musculature represent two independent systems as there are no muscle bundles connecting the two types of cavities. The atrioventricular bundle is the only connection system between the atrial and ventricular musculature.

The ventricular musculature presents a very complex organisation that is not yet fully defined in detail. However, also in the ventricles one can distinguish a specific musculature for each cavity and a common one. Three overlapping layers can be identified in the ventricular musculature (Figure 1.2). In the subepicardial position there is a muscular sac common to the two ventricles, formed by the superficial descending portion of the common systems, anterior and posterior. The second layer is formed by the two pockets, one for each ventricle, made up of its own fibers. The third layer is given, in each ventricle, by the continuation of the superficial common systems that, after becoming deep, assume an ascending course. In the constitution of this layer, on the right, sutural fibers also participate; on the left, these fibers are mixed with their own fibres [2].

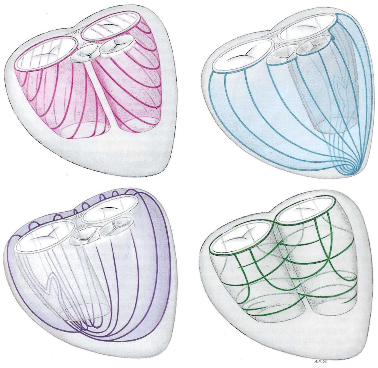

Figure 1.2: Schematic representation of the ventricular musculature layers [2].

1.1.3 Heart conduction system

The conduction system consists of specific myocardial tissue, which can be distinguished from the common myocardium, that forms the cardiac musculature, due to its histological characteristics.

The conduction system (Figure 1.3) includes the sinus node, the atrial conduction tissue, the atrioventricular node, the atrioventricular bundle, and its intraventricular branches.

The sinoatrial node (SA node) represents the heart pacemaker, as the contractile stimulus responsible for the heartbeat originates from it and spreads rhythmically and autonomously. It is located in the thickness of the right atrium wall immediately next to the outlet of the superior vena cava and consists of small, densely packed myocardial specific elements (i.e., nodal cells).

The atrial conduction tissue aids the rapid propagation of the impulse to the atrial myocardium and leads it to the AV node.

The atrioventricular node (AV node) is located on the right side of the basal part of the interatrial septum. It is characterised by very slow propagation of the impulse, which thus reaches the ventricle after a significant delay, and whose cells possess marked pacemaker activity such that, in the absence of the impulse from SA node, AV node is able to maintain a rhythmic and functionally effective contraction of the ventricles.

The atrioventricular bundle (i.e., bundle of His), after its origin from the node of the same name, reaches the interventricular septum and divides into two branches: right and left bundle. The nodal cells, as they move away from the atrioventricular node, run parallel to each other and increase in volume, until they gradually take on the appearance of typical (i.e., giant) Purkinje cells in its branches.

The contractile wave in the ventricles propagates from the apex towards the base and from the subendocardial region towards the subepicardial one, (i.e., from inside the cavities towards the surface).

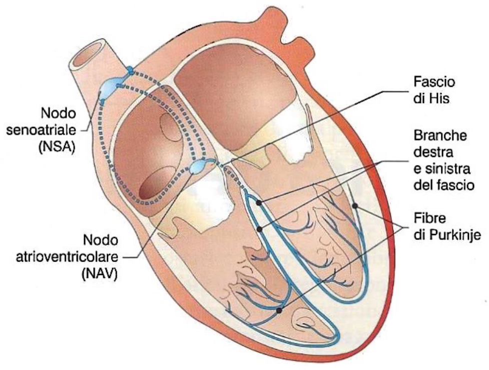

Figure 1.3: Heart conduction system [2].

The contractile stimulus that underlies cardiac automatism can arise at any level of the conduction system, but the specific part of the tissue that possesses the highest frequency of automatism takes on the role of true pacemaker, imparting its rhythm to the entire cardiac mass and blocking the activity of other excitation centres.

Since in the components of the conduction system located below the sinoatrial node the frequency of stimulus onset is lower than that of the node itself, decreasing progressively as one approaches the tip of the heart, it follows that under normal conditions it is the sinoatrial node that assumes the role of true pacemaker. From the latter, in fact, the contractile stimulus autonomously originates and spreads to the atria and then through the atrioventricular system to the ventricles. The resulting rhythm is called sinus rhythm with an average resting frequency of 60-70 beats per minute.

When the sinoatrial node is unable to play the role of pacemaker, due to the excessive slowing down of the frequency of its excitatory discharges or the impossibility of propagating its stimuli (i.e., sinoatrial block), the atrioventricular node comes into play as pacemaker, imposing its rhythm of 50-60 beats per minute on the heart.

The occurence of an additional heartbeat (i.e., an extrasystole) can manifest even in individuals who are in good health. It is a premature contraction of the heart that interrupts the normal cardiac rhythm and originates from an ectopic centre, which therefore momentarily assumes the function of a pacemaker. Extrasystoles may be sporadic or grouped in pairs, triplets or larger groups and may originate from centres located in the atria or in any case above the bifurcation of the atrioventricular bundle (i.e., supraventricular extrasystoles), as well as from centres located in the ventricular myocardium (i.e., ventricular extrasystoles) [2].

1.2 Mechanics of heart contraction

The cardiovascular system consists of a central pump, the heart, and cylindrical conduits, the vessels, whose function is to transport blood from the centre to the periphery and from the periphery to the centre. In particular, there are two mechanical pumps: the right one, constituted by the right ventricle, that gives rise to the pulmonary circulation (or small circulation), and the left one, represented by the left ventricle, that gives rise to the systemic circulation (or large circulation).

The heart pumping function consists of filling the ventricles with blood coming from the atria and subsequently emptying into the arteries. These two phases are called ventricular diastole and ventricular systole. The sequence of mechanical events that affects the right ventricle is similar to that which occurs in the left ventricle, only the levels of pressure that develop in right systole (i.e., 25-30 mmHg) change from those that occur on the left (i.e., 120 mmHg).

Ventricular diastole begins with the closure of the aortic semilunar valve when the intra-aortic pressure exceeds the intraventricular one, followed by isovolumetric ventricular relaxation (i.e., isovolumetric diastole). In this way, the wall tension is reduced and the intraventricular pressure decreases. The pressure drop is rapid, so that the intraventricular pressure becomes lower than the intra-atrial one. At this point, due to the pressure gradient between the atrium and ventricle, the atrioventricular (i.e., mitral) valve opens and blood flows from the atrium into the ventricle. The ventricular cavity enlarges as the fibers stretch. When the ventricle is about 85% full of blood, atrial systole occurs, which completes ventricular filling.

When ventricular systole intervenes, the mitral valve leaflets are pushed towards each other by the blood filling the ventricle and are pressed together. When the intraventricular pressure of the blood exceeds the intra-aortic pressure, the opening of the semilunar valve occurs, allowing blood to flow from the ventricle into the aorta. In the heart of a healthy adult man, the pressure rises until it reaches values of 120 mmHg. The outflow of blood from the ventricle is accompanied by a reduction in intraventricular pressure, but ventricular ejection (i.e., reduced ejection) continues, until the prevalence of total energy of blood from the ventricle is exhausted. Then, with aortic pressure higher than intraventricular one, blood from the aorta tends to flow back towards the ventricle, but as it flows along the arterial wall it fills and distends the valve leaflets, causing them to close again. At this point, ventricular diastole begins. Both the semilunar and atrioventricular valves are closed as the wall tension begins to fall and the cardiac cycle begins again.

Under physiological conditions, the volume of blood put into circulation by the left ventricle in an adult male is about 70 ml: this volume of blood is called systolic output. At the end of ventricular systole, a volume of about 50-60 ml remains in the ventricle, which is called the telesystolic volume [13].

1.3 Electrical conduction in the heart tissue

The mechanical activity of the heart is initiated by the propagation of an action potential both through the conduction system and in the muscular tissue, which constitutes a functional syncytium with electrical continuity through gap junctions between one cell and another. A portion of the conduction system is organised in such a way that the electrical impulse propagates very slowly: this allows the atrium to efficiently contract while the impulse is delayed, before passing through the fibrous septum that separates atria from ventricles, in the atrioventricular node. This allows the atrial contraction to effectively end while the ventricle is released. The impulse then rapidly spreads to the ventricular musculature resulting in contraction and emptying of the ventricle.

The SA node cells depolarize at rest until they reach the action potential discharge threshold and then discharge automatically and rhythmically. The bioelectric characteristics of the cells of the conduction tissue determine both the heart rate and the speed of impulse propagation and the resulting delay between atrium and ventricle.

The currents during the action potential, which are regulated and differ in the various myocytes, determine the duration of depolarization and, consequently, the input of calcium (Ca^{2+}) and the intensity, speed, and duration of muscle contraction. The main regulations of the electrical characteristics concern the pacemaker current (I_f) and the activity of voltage-dependent Ca^{2+} channels [13].

1.3.1 Action potential of cardiac cells

Cardiac cells express a considerable number of voltage-dependent conductances, with varying kinetic characteristics, which allow the cell itself to give rise to different trends in membrane potential following activation, generating action potentials of very different forms and with different functional consequences [13].

Phases of action potential

Five phases are distinguished in the description of the cardiac action potential (Figure 1.4): i) rapid depolarization, ii) early partial repolarization, iii) *plateau*, iv) repolarization, and v) diastolic depolarization.

Rapid depolarization (i.e., phase 0) occurs in response to exceeding

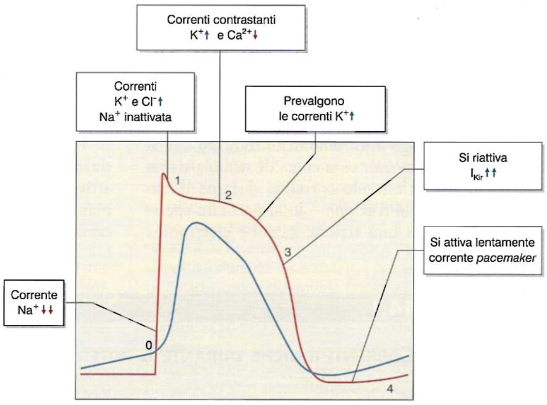

Figure 1.4: Action potential of cardiac cells [13].

the threshold for the opening of sodium channels. This phase is sustained by an intense sodium (Na^+) current and is self-limiting due to the rapid inactivation of the channels themselves. Phase 0 is only evident in cardiac cells that express significant levels of Na^+ conductance and are called fast cells.

Early partial repolarization (i.e., phase 1) is caused by the concomitant inactivation of Na^+ channels with the transient activation of a potassium (K^+) current (i.e., transient outward current, I_{Kto}) and a chlorine (Cl^-) current (in Purkinje cells in particular). Phase 1 is only evident in cardiac cells that have a clear phase 0 and in which the K^+ transient conductances are significant.

The plateau (i.e., phase 2) is determined by the activation of voltage-dependent slow Ca^{2+} conductances (which generate a slow inward current, I_{si}) counterbalanced by the slow activation of voltage-dependent K^+ conductances (which generate I_{Kr} or delayed rectifier) that produces a more or less prolonged equilibrium between Ca^{2+} conductances, which tend to depolarize the membrane, and K^+ conductances, which tend to repolarize it.

Repolarization (i.e., phase 3) occurs due to the gradual inactivation of Ca^{2+} conductances, as opposed to a gradual increase in K^+ currents. From the momentary plateau equilibrium, a process of rapid and complete repolarization takes place, due to two important concomitant and self-amplifying factors: the closure of Ca^{2+} conductances as repolarization proceeds (closure that contributes to repolarization) and the activation of K^+ conductances, active at rest, that depolarization had switched off and that are reactivated as the cell repolarizes (i.e., inward rectifier K^+

currents, K_{ir}).

With regard to the diastolic depolarization or resting phase (i.e., phase 4), the cell can show a more or less marked, gradual depolarization, which can reach the threshold and lead to the initiation of a new action potential. The intensity of this process depends on the degree of expression of a cationic conductance called pacemaker current (I_f). The current generated by the Na/Ca^{2+} exchanger also contributes to depolarization in phase 4, which can be influenced by cyclic processes of local Ca^{2+} release at the sarcolemma by the sarcoplasmic reticulum (i.e., intracellular clock). Diastolic depolarization is only present in the cells of the conduction tissue and not in cardiac myocytes, which instead have a resting phase 4. Furthermore, the automatic initiation process of the action potential will only occur in the pacemaker cells because the others will be invaded by the propagated action potential before they can reach the threshold on their own.

Refractoriness

The inactivation of Na^+ currents following depolarization persists until the membrane resumes its correct polarization. Therefore, during the prolonged cardiac action potential, the Na^+ channels are inactivated and will not become available to generate a new action potential as long as the cell remains depolarized. This gives rise to a phenomenon referred to as refractoriness: trying to stimulate a cardiac fiber, by injecting current, during its normal action potential will only produce passive responses, until an adequate number of Na^+ channels have emerged from the inactivated condition, so that an active response can be initiated.

In particular, as long as the cell is highly depolarized, no active response will be evoked (i.e., absolute refractory period). As the membrane repolarizes, an increasing number of Na^+ channels will come into play producing an active response, which will become more and more pronounced. Only if the number of active Na^+ channels is sufficient, however, the active response will be able to depolarize a larger membrane region to the threshold value for Na^+ channels, initiating an active response in the surrounding area as well and thus allowing the impulse to propagate. Until then, from a functional point of view there will be a condition of effective refractoriness, because the impulse cannot propagate, although an active response is present. When, on the other hand, the active response becomes able to propagate, there is no longer a condition of effective refractoriness, but the response will still remain reduced and altered until all Na^+ channels are functional again. Until then, the cell will be in a condition of relative refractoriness. A representation of the refractory states of the cardiac cells is illustrated in Figure 1.5.

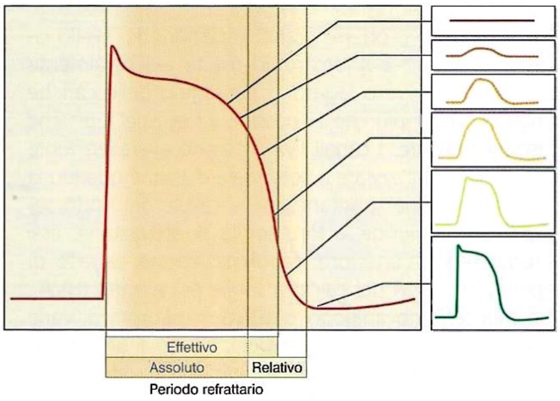

Figure 1.5: Representation of the refractory states of the cardiac cells [13].

A similar situation is also found in cells that have no Na^{+} channels and base the action potential on voltage-dependent Ca^{2+} channels. Also in this case channel inactivation is observed, which contributes to the action potential switching off. In fact, if Ca^{2+} channel kinetics is slower, inactivation lasts longer. Thus, slow cells also exhibit refractoriness. Typically, the relative refractoriness extends beyond complete repolarization, so that the ratio of refractory period to action potential duration is greater in this type of cell.

The fundamental consequence of relative refractoriness is to alter the impulse conduction velocity.

1.3.2 Physiological and pathological factors influencing cardiac electrical activity

The physiological range of variability of the pacemaker discharge frequency at rest is quite wide (e.g., 60/100 beats per minute). An excessively slow or excessively fast heart rate (i.e., tachycardia) is usually an indication of cellular distress in the SA node, either primary or secondary to infection, metabolic or connective tissue disease, or resulting from altered ionic conditions. Variations in heart rate, generally characterised by rhythm irregularities (i.e., arrhythmias), may arise as a result of the onset of automatic activity outside the sinoatrial node (i.e., ectopic foci of automatism), in the presence of conduction disturbances, or due to the concomitance of both alterations [13].

Conditions for the occurrence of sustained arrhythmia

It is important to recognise that the occurrence of a premature beat, although it may often be perceived by the subject himself as a discontinuity in the heart rhythm, does not in itself constitute a particularly serious problem: even if the ventricle performs a cycle without having filled up properly, the interference with the pumping and perfusion activity of the tissues is marginal and it is quickly compensated for by the subsequent pulsations. The situation in which the premature beats become frequent is dangerous, because the pump function is compromised. There are two general situations in which a premature impulse sustains indefinitely: firstly, phenomena related to the variability of cardiac cycle duration and action potential, in particular regional differences in the process, and secondly, the concomitance of the discharge of an ectopic focus (or at least the genesis of premature impulses) with alterations in conduction.

In the course of the normal cardiac cycle, the succession of phases of normal excitability and phases of relative or absolute refractoriness continuously determines variable conduction properties. Consequently, while the impulse that invades the cardiac tissue at rest may propagate in the correct manner and involve all the cells in the correct sequence, a premature impulse may find different cell groups in different conditions of relative refractoriness and undergo a more or less marked slowing of conduction that varies from one region of the heart to another.

Re-entry mechanisms

In order for an abnormal automatic activity to give rise to an arrhythmia that is sustained indefinitely, it is sufficient for an impulse, instead of invading the entire cardiac musculature in sequence and exhausting itself once the whole heart has been excited, to find a way to propagate itself in a closed path through the cardiac tissue, so that it returns to invade the region where it was originally produced and can propagate again along the same route.

Generally, the conduction speed of the impulse in cardiac tissue is such that, whatever pathway the impulse follows to return to a region that has already been activated by its passage, it arrives there while the tissue is still refractory. On the other hand, under conditions of relative refractoriness, the conduction velocity can be greatly reduced. Therefore, if the impulse moves along a closed pathway invading the tissue as soon as it becomes excitable (but is still in relative refractoriness), it will propagate slowly. It can thus continue to find tissue exiting the refractory period in front of it and, consequently, circulate indefinitely, activating the cardiac muscle at even very high frequencies (e.g., above 300/s).

This clarifies how an ectopic premature impulse can initiate an arrhythmia that is sustained over time. In fact, arrhythmias generated by this mechanism are called re-entry arrhythmias.

Fibrillation

Fibrillation is a situation of desynchronization of the activation and contraction of different regions of the heart muscle. Failure of the ventricular muscle mass to contract synchronously is incompatible with normal circulatory function and therefore with life.

In order for ventricular fibrillation to occur, many causes must be involved: more than one re-entry mechanism must be initiated at the same time, so that several impulses travel simultaneously through different regions of the heart.

In the presence of tissue necrosis, surrounded by tissue that is electrically unexcitable or otherwise depolarized and with greatly altered characteristics of impulse conduction and refractoriness, a premature impulse may find considerable differences in the conditions of polarization and excitability between cells and pass through the region surrounding the infarct, leaving many cells unexcited and creating possible multiple re-entry pathways. Ventricular fibrillation is, in fact, the most serious complication of a myocardial infarction that does not destroy a portion of muscle mass large enough to impair the heart mechanical function.

The difference between cells in the timing and pattern of repolarization and recovery from the actual refractory period is, therefore, a predisposing condition for the onset of fibrillation in response to a premature impulse.

1.4 Myocardial infarction: complications and treatments

Myocardial ischemia is the suffering or damage of myocardial cells resulting from an insufficient supply of oxygen with respect to their metabolic demands.

In Italy, cardiovascular diseases are the cause of approximately 45% of global mortality, and, among these, ischemic heart disease is responsible for 35% of deceases, with an annual death toll of approximately 130,000. Coronary atherosclerosis is by far the most frequent cause of ischemic heart disease, although not the only one, and ischemia generally affects mainly the subendocardial layers, which are more exposed than the subepicardial ones. Another cause of ischemia, for example, is coronary artery spasm, characterised by intense vasoconstriction of a segment of one or more epicardial coronary vessels, leading to occlusion of the vessel lumen resulting in a severe reduction in oxygen supply to the myocardium. This oxygen deficiency usually affects the entire thickness of the myocardial region supplied by the vessel (i.e., transmural ischemia) [54].

1.4.1 Consequences of myocardial ischemia

Ischemia causes major myocardial alterations that usually occur according to a typical time sequence, known as the ischemic cascade, which involves, in a short time, first the metabolic, then the mechanical and then the electrical activity of myocardial cells. Finally, ischemic cardiac pain may appear in the patient, but not always. These changes are reversible if the ischemia is transient. If it is prolonged beyond 20-30 minutes, the cellular alterations become irreversible, necrosis of the ischemic area occurs, and it's called myocardial infarction.

If myocardial necrosis develops, the contractile dysfunction of the region affected by the ischemic damage will become persistent. The greater the extent of the infarcted area, the greater the degree of contractile function impairment of the left ventricle and thus of the heart. Myocardial ischemia alters not only ventricular contraction, but also ventricular relaxation, hindering normal ventricular filling.

The site of a myocardial infarction depends on the occluded coronary artery, but usually necrosis affects the left ventricular and septal myocardium. The thickness of the cardiac wall in the infarcted area appears reduced as a result of myocardial tissue necrosis and, over the course of 3-4 months, the infarcted area becomes a hard, retracted scar. The time required for complete replacement of the necrotic tissue and scarring depends on the size of the infarct.

Myocardial ischemia significantly alters the electrical properties of myocardial cells, many of which are maintained by energy (and thus oxygen) consuming ion pumps, causing abnormalities in the depolarization and/or repolarization phase, which are reflected on the electrocardiogram. Acute ischemia of the myocardium can cause an alteration in the depolarization phase, with a reduction in the amplitude of the action potential and a slowing of the rising velocity (i.e., phase 0), which results in a slowing of the depolarization of the ischemic region. At the same time, there is a reduction in the duration of the action potential, with a shortening of phases 2 and 3. Furthermore, the repolarization process of ischemic myocardial cells may be incomplete, so that the resting membrane potential may be around -70 mV instead of the normal -90 mV. These alterations generate a potential difference between healthy and ischemic tissue, and thus abnormal currents from one tissue to the other. When necrosis of a myocardial region (i.e., infarction) occurs, it no longer contains electrically active cells.

In patients with previous infarction, especially if complicated by left ventricular dysfunction, ventricular fibrillation and sudden death are more frequently due to mechanisms that are independent of the occurrence of ischemia and more related to arrhythmic phenomena favoured by the inhomogeneity of depolarization and repolarization processes in peri-infarct areas with electrophysiological abnormalities of myocardial cells [54].

1.4.2 Treatments

At present, there are no clinical methods to treat an acute myocardial infarction, but mostly there are procedures to prevent aggravation of the condition of the patients suffering from chronic ischemic heart disease. The objectives of treating these patients are twofold and are related to reducing the risk of serious coronary events (e.g., death, infarction) and reducing the severity of ischemia.

The pursuit of these goals is based first and foremost on lifestyle correction with the aim of reducing cardiovascular risk factors (e.g., abstaining from smoking, limiting the body mass index, doing regular physical activity), but also on the use of drugs that corrects cardiovascular risk factors, in particular hypercholesterolaemia, hypertension and diabetes, when lifestyle optimisation has not been sufficient to achieve this.

Other methods to improve the condition of high-risk patients are percutaneous myocardial revascularization (i.e., coronary angioplasty) and coronary artery bypass.

Numerous scientific articles consulted indicate that there are currently no devices or technologies that can be used to repair and treat the infarcted area of the myocardium, except for a few solutions that only aim to regenerate damaged cardiac or vascular tissue, for example pericardial closure, valve and annulus repair and great vessel reconstruction [8, 9, 24, 29]. Other companies are exploring the application of technologies based on stem cells to treat acute myocardial infarction, but these studies are still at the stage of clinical trial [26].

1.5 State of the art on cardiac patches

The devices approved for clinical use that were cited in subsection 1.4.2 are not curative, they provide only limited tissue regeneration and are not capable of establishing electrical integration with the tissue [8].

A promising new field of study is that of myocardial tissue engineering, which uses hydrogels, scaffolds and patches to support and replace damaged tissue with cellular and non-cellular approaches [5, 22, 30, 41, 58, 67].

Focusing on acellular patches, just as it is important to restore the electrical characteristics of the infarcted tissue area, it is also necessary that the patch applied to the heart tissue does not compromise the regular function of this organ. Therefore, the mechanical characteristics of the patch must resemble those of the heart tissue as closely as possible, altering only slightly the state of deformation established during the cardiac cycle [21].

The spatial organisation of the muscle fibres of the cardiac tissue allows simultaneous contraction or expansion of the organ in both transverse and longitudinal directions, with a volumetric deformation up to 20% [7, 9, 14]. This characteristic is also refferred to as auxetic surface of organs.

Cardiac tissue exhibits a Poisson's ratio between -0.8 and -0.6 (i.e., transverse strain is 60-80% of longitudinal one) and a conductivity of 0.3-0.6 S/m [8]. Other studies state that the Poisson's coefficient may lie between -0.5 and -0.2 [9], and electrical conductivity could fall between 0.5 S/m and 0.8 S/m in transverse direction, and between 0.15 S/m and 0.3 S/m in the longitudinal one [14].

Therefore, patch geometries that can match the anisotropy of the heart tissue are, for example, the re-entrant honeycomb, the arrowhead, and the sinusoidal ligament architectures [8, 9]. Conductivity, on the other hand, can be imparted by coating the patch with polyaniline, or polypyrrole or the addition of gold or selenium nanoparticles [8].

Among the patch parameters to be checked there is the transverse-longitudinal stiffness ratio. Indeed, as already mentioned, cardiac tissue is characterised by an intrinsic anisotropy, such that it exhibits a transverse stiffness of 0.1-0.5 MPa and a longitudinal stiffness of 0.05-0.25 MPa (i.e., the former being 2-4 times the latter) [9].

1.5.1 Geometries

The most promising patch designs are the auxetic ones and have the characteristics of being highly deformable, resistant to shear, resilient and having an anisotropy ratio that can be modified by varying the geometric parameters of the unit cells. They can be divided into three main categories: i) re-entrant structures, ii) chiral structures, and iii) rotating unit structures [34, 66].

Among the re-entrant designs (Figure 1.6) there are honeycomb, star-honeycomb, missing rib, arrowhead, sinusoidal ligaments, lozenge grid [34]. If classical auxetic geometry are to be used, the best for cardiac patches are those with honeycomb and arrowhead structures because they are closer to cardiac tissue in terms of mechanical properties [9]. Honeycomb structures have a high deformation at break and together with the arrowhead have a higher transverse/longitudinal stiffness ratio than the other architectures [9]. The missing rib has the lowest Young's modulus, which is closer to that of the myocardium and is inherently anisotropic [66].

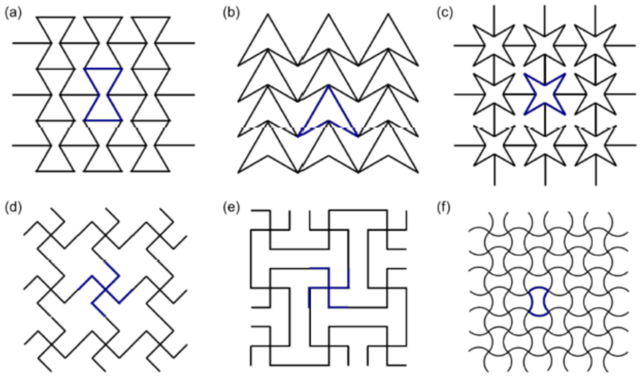

Figure 1.6: Re-entrant structures. (a) Re-entrant honeycomb, (b) double arrowhead, (c) star honeycomb, (d) missing rib, (e) lozenge grid, (f) sinusoidal ligaments [34].

Structures with rotating units (Figure 1.7) have units with different geometric shapes connected at some of the vertices and when they deform, they rotate around them. There are different types of units: squares, triangles, rectangles, rhombuses and tetrahedra. Those with squares, in particular, have a large elongation capacity and a negative Poisson's coefficient that can be adjusted according to geometric parameters. Those with triangles have greater stiffness in the transverse direction than in the longitudinal one, and the anisotropy ratio can be modified [66].

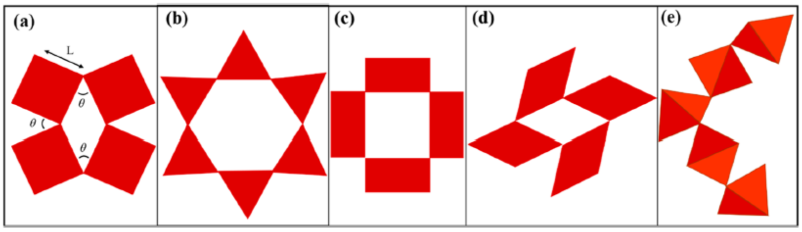

Figure 1.7: Rotating unit structures. (a) Square unit cells, (b) triangle unit cells, (c) rectangle unit cells, (d) rhombus unit cells, (e) tetrahedron unit cells [66].

In chiral structures (Figure 1.8), straight ligaments are connected to the central node, that rotates and causes wrapping or unwrapping. The negative Poisson's ratio remains constant if the length of the ligaments and the radius of the node increase. Its magnitude increases if the radius of each node and the radius between the nodes increase, but the stiffness of the structure decreases, while Young's modulus increases with the increasing of ligament thickness [66].

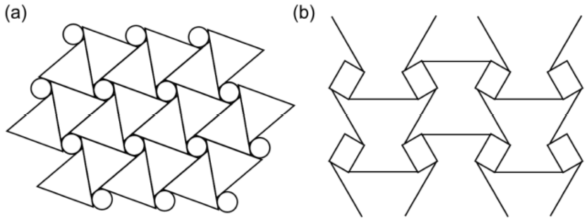

Figure 1.8: Chiral structures. (a) Chiral structure with same units, (b) Chiral structure with symmetrical units [34].

1.5.2 Materials

The most commonly used materials can be either non-conductive or conductive, and often a combination of the two is used.

Non-conductive materials include natural materials (decellularized extracellular matrices and certain polymers such as collagen, algin, fibrin, chitosan and hyaluronic acid) and synthetic materials, such as polyethylene (PE), polypropylene (PP), polyethylene glycol (PEG), polyglycerol sebacate (PGS), polycaprolactone (PCL), polylactic acid (PLA), poly(lactic-co-glycolic) acid (PLGA), poly-L-lactic acid (PLLA), polyurethane (PU), polytetrafluoroethylene (PTFE) [33, 66].

Conductive materials are divided into intrinsically and extrinsically conductive. The former are polymers such as polypyrrole (PPy), polyaniline (PANi), polythiophene (PT), and derivatives such as polyethylenedioxythiophene (PEDOT). They are conductive due to the movement of electrons in the molecular chains. The latter consist of a non-conductive matrix to which a conductive filler is added, such as carbon-based materials (graphene, graphene oxide, reduced graphene oxide, carbon nano-tubes (CNT) and carbon nano-fibres), or metallic nanoparticles of gold, silver, titanium carbides [31, 37, 38, 61].

To pick one, PGS has mechanical and degradation characteristics that can be adjusted by adjusting the percentages of glycerol and sebacic acid. In general, its properties are close to those of myocardium and its cost is limited. An example are films of (non-conductive) PGS coupled with 1% graphene [60].

Conductive polymers are generally cytotoxic at high concentrations and polypyrrole has low adhesion to cardiac tissue [21]. If adhesiveness was to be increased, some cases were found where GelMA (i.e., gelatin methacrylate) was added [6, 7]. Some examples are PCL + PPy, PANi + chitosan, PU + PANi + silicon dioxide [49]. Metallic nanoparticles are easy to synthesise but have problems with biocompatibility at high concentrations as do carbon nanotubes.

1.6 Objective of the thesis

In the context of research aimed at improving the condition of heart attack patients, the objective of this thesis is to study the design of an auxetic cardiac patch capable of conducting electrical signals while minimizing the impact on the mechanical functionality of an infarcted ventricle, addressing first the mechanical aspect, then the electrophysiological one.

The first step constists in verifying the possibility of using an optimization tool to obtain a patch geometry that has mechanical properties consistent with those of cardiac tissue. This is in opposition with the existing geometries studied in literature and exposed in subsection 1.5.1 that require the modification of geometric parameters to make their mechanical properties as close as possible to those of the heart through an iterative process.

Once the structure of the patch has been obtained, the following step will consist in studying its behavior in the mechanical field to analyze whether auxeticity is an advantage over using a material with a positive Poisson's ratio and evaluate how much its presence affects the deformations of the heart during the cardiac cycle, using simplified and non-simplified heart models.

Regarding the electrophysiological aspect, the objective is to examine the conductivity of the patch in terms of its ability to conduct the electrical signal transmitted by myocardial cells, both in the case of a physiological beat and in more abnormal situations, such as the presence of an extra systole.

Chapter 2

Patch geometry definition

2.1 Optimization tool

Most of the studies found in literature [8, 9, 32] showed that an adequate patch must have mechanical and electrical properties as similar as possible to those of the healthy myocardial tissue. Since the infarcted tissue is way more rigid than the healthy tissue, a thin patch can't give any support to the structure. Being put in parallel to the infarcted area, all the stresses would be carried by the damaged region and not by the patch. Since the device is unable to give mechanical support, the aim is to realize a patch that doesn't interfere with the mechanical properties of the heart, hence giving to it similar properties.

If on one hand the geometry can simply be that of a square or a rectangle with a certain thickness, for example 1 mm, on the other hand more attention should be paid to the geometry of the device. In fact, if the overall behavior of the heart tissue is auxetic, the patch must be formed by a series of repeated unit cells whose macroscopic response is auxetic as well [32].

For the definition of patch geometry, a topology optimization tool was used [20] and it was run on *FreeFEM* (Pierre and Marie Curie University, Paris, 2020). This tool allows to design lightweight structures that respect the required properties in terms of mechanical behaviour and thermal conductivity behaviour. The latter can be interchanged with the electrical behaviour since the equations governing the two physical contexts are analogous. Hence, this work focused on finding the best geometry that fitted the mechanical properties and electrical conductivities required for the patch to be matched with the heart tissue.

The inputs to the tool were the bulk material properties (i.e., Young's modulus, Poisson's coefficient, and electrical conductivity) and the patch requirements, in terms of homogeneous mechanical properties and electrical conductivity.

The code started creating a cell with a random density distribution and a uniform mesh as it is seen in Figure 2.1.

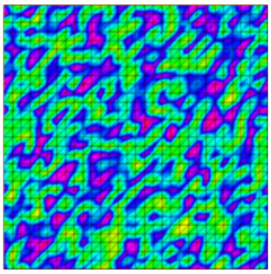

Figure 2.1: Starting cell of the optimization code with a random density distribution and a uniform mesh.

Then, the optimizer iterations began, followed by filtering and mesh adaptivity phases. These operations were performed iteratively until the mesh error was less than the imposed mesh tolerance or until the established maximum number of mesh adaptivity iterations was reached. As an output the tool gave the topology of the cell, with a specific density distribution which satisfied the boundary conditions that were imposed. An example is shown in Figure 2.2.

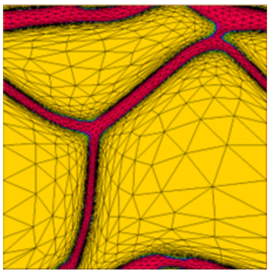

Figure 2.2: Example of final density distribution in a unit cell. The mesh is refined where the density is higher (red coloured region), and it is coarser where the density has a value close to zero (yellow coloured region).

The optimization tool allowed to directly set a range of interest for the elements of the stiffness matrix E, which is the inverse of the compliance matrix C.

$$E = \begin{bmatrix} E_{1111} & E_{1122} & E_{1112} \\ E_{2211} & E_{2222} & E_{2212} \\ E_{1211} & E_{1222} & E_{1212} \end{bmatrix} = C^{-1}$$

For orthotropic materials, the compliance matrix C consists of elements that depend on the Young's modulus, the stiffness ratio and the Poisson's coefficient.

$$C = \begin{bmatrix} \frac{1}{E_1} & \frac{-\nu_{21}}{E_2} & 0 \\ \frac{-\nu_{12}}{E_1} & \frac{1}{E_2} & 0 \\ 0 & 0 & \frac{1}{G} \end{bmatrix} \tag{2.1}$$

where E_1 is the transverse stiffness, that in the contest of this thesis indicates the circumferential direction of the heart fibres, E_2 is the longitudinal stiffness, G is the shear modulus, and ν_{12} and ν_{21} are the Poisson's ratios in fibres direction (i.e., the one of interest) and longitudinal direction, respectively.

Electrical conductivity properties were controlled through the elements of k matrix.

$$k = \begin{bmatrix} k_{11} & k_{12} \\ k_{21} & k_{22} \end{bmatrix}$$

where k_{11} is the transverse conductivity, and k_{22} the longitudinal conductivity.

Starting from the mechanical and conductive properties of the heart found in literature, the requirements used for the topology optimization were:

- **Young's modulus**:

  $$E_1 = 0.1 \div 0.5 \, MPa$$
  $$\frac{E_2}{E_1} = 0.25 \div 0.5$$

  An arbitrary value was chosen for the shear modulus G due to lack of information found in literature.

- **Poisson's ratio**:

  $$\nu_{12} = -0.8 \div -0.2$$

- **Electrical conductivity**:

$$k_1 = 0.2 \div 0.8\, S/m$$
$$\frac{k_2}{k_1} = 0.3 \div 0.8$$

While conductivity can be controlled in a direct way in the optimization tool, the mechanical properties can't. To set the requirements, i.e., to get the ranges of constraints for the elements of the stiffness matrix, computations were conducted starting from average values of the mechanical properties.

$$E_1 = 0.3\, MPa$$
$$\frac{E_2}{E_1} = 0.375 \rightarrow E_2 = 0.1125\, MPa$$
$$\nu = -0.5$$

The elements that needed to be controlled in this case were E_{1111}, E_{1122} and E_{2222}. Substituting the average values of the mechanical properties in the compliance matrix and then inverting it using *Matlab* (The MathWorks Inc., Massachusetts, United States, 2018), the values of the stiffness matrix were obtained.

$$C^{-1} = \begin{bmatrix} 0.3310 & -0.0621 & 0 \\ -0.0621 & 0.1241 & 0 \\ 0 & 0 & 0.05 \end{bmatrix} = E$$

The requirements were given through a range of values, that was computed considering the lower and upper limits proportional to the lower and upper limits of the heart tissue properties. For instance, the average value of E_1 was 0.3 MPa, and its lower and upper limits were 0.1 MPa and 0.5 MPa, which were respectively the average value minus its 66% and the average value plus its 66%. Hence, to obtain the correspondent range of values for E_{1111}, the 66% of the average value of E_{1111} obtained in *Matlab* was removed from and added to itself to get the lower and upper limits of this element. Thus, obtaining:

$$0.11\, MPa < E_{1111} < 0.55\, MPa$$

The same procedure was done for all the matrix elements of interest. For the element E_{1122} the Poisson's coefficient range of values was used, since

E_{1122} depends on it and on E_{1111}, for which the range was already specified. For the element E_{2222}, the range of the stiffness ratio was used. The results obtained were:

$$-0.099\,MPa < E_{1122} < -0.025\,MPa$$

$$0.25 < \frac{E_{2222}}{E_{1111}} < 0.5$$

For the conductivity values, the ranges found in literature were used, because the transverse conductivity and the conductivity ratio were directly controllable through the elements of the k matrix, obtaining:

$$0.2\,S/m < k_{11} < 0.8\,S/m$$

and

$$0.3 < \frac{k_{22}}{k_{11}} < 0.8$$

The diagonal terms were not of interest.

The simulations gave as an output the elements of the stiffness matrix and of the conductivity matrix of the unit cell.

Concerning conductivity, the values of interest were k_1 and k_2, directly extracted from the k matrix given as output of the optimization code, and through these the conductivity ratio was easily derived.

Regarding the mechanical properties, the useful parameters were E_1, E_2 and ν. However, these were not directly corresponding to the values of the stiffness matrix elements in output from the optimization code, so they were obtained performing some simple calculations on *Matlab*. First, the stiffness matrix E was imported and inverted so as to obtain the compliace matrix C. From the elements of the latter, via Equation 2.2, Equation 2.3, Equation 2.4, the desired properties of the cell were obtained. Thus, being

$$C = \begin{bmatrix} C(1,1) & C(1,2) & C(1,3) \\ C(2,1) & C(2,2) & C(2,3) \\ C(3,1) & C(3,2) & C(3,3) \end{bmatrix}$$

then,

$$\nu_{12} = -\frac{C(2,1)}{C(1,1)} \tag{2.2}$$

$$E_1 = \frac{1}{C(1,1)} \tag{2.3}$$

$$\frac{E_2}{E_1} = \frac{C(1,1)}{C(2,2)} \tag{2.4}$$

To make these equations valid, the elements E_{1112}, E_{2212}, E_{1211}, E_{1222} of the stiffness matrix must be close to zero. While E_{1222} and E_{2212} were already very close to this value in all simulations, it was necessary to impose an additional constraint on the value E_{1112} so that the matrix structure was the same as shown in Equation 2.1. Only one constraint was imposed by exploiting the symmetry of the matrix and taking into account that the simulations in general performed better the smaller the number of constraints was.

If the results did not fall within the imposed ranges, the constraints were slightly modified deviating from the original ones. This means that if, for example, the value of E_{1111} was below the lower constraint, this value was raised “forcing” the simulation to respect it. In addition to these adjustments, other parameters were changed to meet the best result, such as the maximum number of meshes on which the filtering was done and the mesh tolerance value.

Once the requirements were specified, the tool needed to know the properties of the bulk material of interest. After some simulations, it was clear how some values of the bulk material properties were too high and made the structure of the cell too thin. For example, by initially entering a Young’s modulus of 6.73 MPa and a conductivity of 16.2 S/m [40], the structure turned out to be extremely thin, as it can be seen in Figure 2.3. This happened because the purpose of optimization was to minimize mass, so if the initial properties were too high, less material was sufficient to meet the constraints.

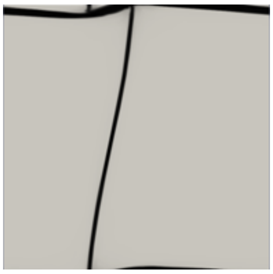

Figure 2.3: Unit cell for PANi, phytic acid and chitosan.

2.2 Results

The objective of this topology definition was to match conductivity and minimize stiffness so to create as little interference as possible with the heart tissue properties and allow the electric signal to flow undisturbed.

However, the optimization tool was based on mass minimization, that was not of particular interest in this case. Therefore, to follow this logic, E_{1111} minimization as objective function could have been a solution. Nevertheless, mass minimization allowed to obtain a structure that was physically reasonable. Without this objective the tool could possibly create a structure with lumps not connected to the main structure or other unreasonable geometries, following the requirement of low stiffness and having no requirement on the mass.

In the following paragraphs, the results obtained by using mass minimization alone and mass minimization concurrently with E_{1111} minimization are shown. This was achieved by customizing the objective function within the original code [20].

2.2.1 Mass minimization

The bulk properties of the materials under consideration that yielded satisfactory results are shown in Table 2.1.

Table 2.1: Bulk material properties of materials under consideration.

	E [MPa]	k [S/m]	ν
1. PANi + PGS [53]	6	1.77	0.4
2. PU + gelatin + CNT [65]	3.27	1.3	0.4
3. PANi + PCL [10]	14.1	1.62	0.4

Table 2.2 illustrates the constraints that, after several adjustments, led to a geometry in accordance with the specified requirements.

As explained in section 2.1, the homogeneous material properties were computed for each cell and are displayed in Table 2.3.

Figure 2.4, Figure 2.5, and Figure 2.6 depict cell structures and their corresponding patterns.

The structure shown in Figure 2.6 is quite complex with respect to the others, and since the aim was to simplify the solution and its realisation as much as possible, this geometry was ruled out.

Table 2.2: Applied constraints for each material.

	E_{1111} [MPa]	E_{1122} [MPa]	E_{2222}/E_{1111}	k_{11} [S/m]	k_{22}/k_{11}
1.	$0.11 \div 0.55$	$-0.099 \div -0.025$	$0.35 \div 0.5$	$0.25 \div 0.8$	$0.35 \div 0.8$
2.	$0.11 \div 0.55$	$-0.099 \div -0.045$	$0.25 \div 0.5$	$0.25 \div 0.8$	$0.35 \div 0.8$
3.	$0.15 \div 0.55$	$-0.099 \div -0.025$	$0.3 \div 0.5$	$0.2 \div 0.8$	$0.3 \div 0.8$

Table 2.3: Homogeneous properties of each material.

	E_1 [MPa]	Poisson	E_2/E_1	k_1 [S/m]	k_2/k_1
PANi + PGS	0.43	-0.23	0.27	0.24	0.35
PU + gelatin + CNT	0.48	-0.35	0.26	0.25	0.35
PANi + PCL	0.51	-0.21	0.31	0.24	0.34

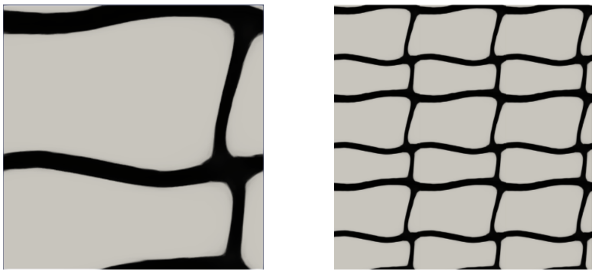

(a) (b)

Figure 2.4: PANi + PGS (a) unit cell, (b) pattern.

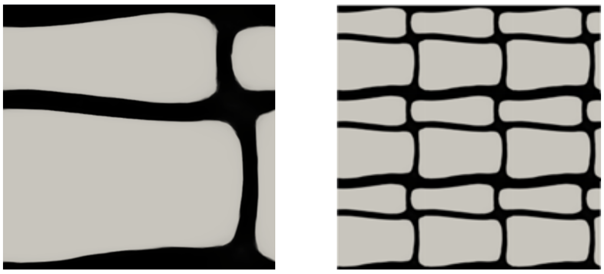

(a) (b)

Figure 2.5: Polyurethane, gelatine and CNT (a) unit cell, (b) pattern.

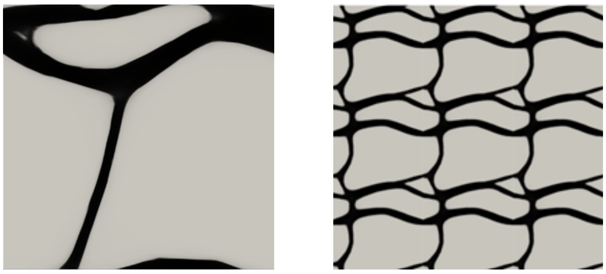

(a) (b)

Figure 2.6: PANi and PCL (a) cell, (b) pattern.

In conclusion, comparing the three solutions in terms of geometry, the first two were simple and quite similar with the advantage that the second had a thicker structure, while the third had the most complex one.

In terms of properties, E_1 was quite similar, always tending to the upper limit. The second structure had a more pronounced auxetic behaviour, while the others had a very similar Poisson's ratio. The stiffness ratio always had a value around 0.3, about halfway between the minimum value and the middle value of the range. The conductivity in the transverse direction and the conductivity ratio had very similar values, always tending towards the lower limits.

2.2.2 Mass and E_{1111} minimization

As seen before, mass minimization alone was not an objective function tailored for this application. However, completely avoiding the objective function of mass minimization didn't lead to any reasonable solution.

One of the purposes of topology definition was to get a robust and easily realisable structure. From a biological point of view, in the perspective of the presence of a transmural infarct, the patch, designed with a realistic thickness of 1 mm, should be able to conduct an electric current equal to that which flows through the ventricle wall. This wall typically presents an average thickness of 10 mm, so the patch must be able to conduct the same current through a thickness ten times smaller. To achieve this target and contemporarily get thicker struts, it was increased the range of constraints for the conductivity of five/ten times the one that was used for mass minimization alone.

The purpose remained to create as little interference as possible with the heart tissue mechanical behaviour. So, a possible solution to achieve this requirement was to delete the constrain on E_{1111}, that was directly correlated to E_1, and introduce an objective function on E_{1111} that minimized it simultaneously with mass minimization.

The bulk properties of the materials under consideration that yielded satisfactory results are shown in Table 2.4.

Table 2.4: Bulk properties of materials under consideration with modified objective function.

	E [MPa]	k [S/m]	ν
1. PANi + PCL + PGS [19]	1.3	6.3	0.4
2. PANi + PCL [19]	2	3.9	0.4

Table 2.5 illustrates the constraints that led to a geometry in accordance with the specified requirements.

Table 2.5: Applied constraints for each material with modified objective function.

	E_{1122} [MPa]	E_{2222}/E_{1111}	k_{11} [S/m]	k_{22}/k_{11}
1.	$-0.099 \div -0.015$	$0.3 \div 0.5$	$1.5 \div 4$	$0.35 \div 0.8$
2.	$-0.099 \div -0.035$	$0.3 \div 0.5$	$1.5 \div 4$	$0.35 \div 0.8$

The homogeneous material properties were computed for each cell and are displayed in Table 2.6.

Table 2.6: Homogeneous properties of each material with modified objective function.

	E_1 [MPa]	Poisson	E_2/E_1	k_1 [S/m]	k_2/k_1
PANi + PCL + PGS	0.25	-0.21	0.30	1.5	0.35
PANi + PCL	0.60	-0.20	0.30	1.49	0.35

Figure 2.7 and Figure 2.8 show cell structures and their corresponding patterns.

From the results in Table 2.6, it can be seen that, by deleting the constraint on E_{1111}, the Young's modulus of the second cell was higher with respect to the case of mass minimization alone, in particular it exceeded the upper limit. This was due to the fact that when a parameter was inside an objective function, the code changed its value freely so to respect as much as possible the imposed constraints.

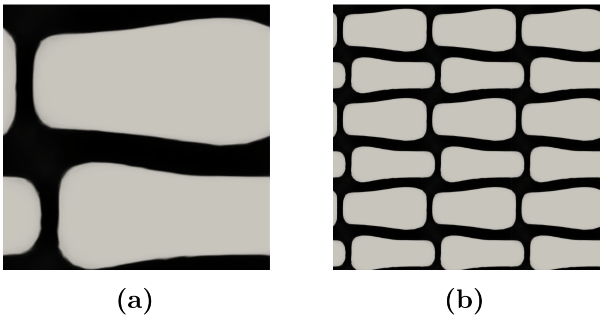

Figure 2.7: PANi + PCL + PGS (a) unit cell, (b) pattern.

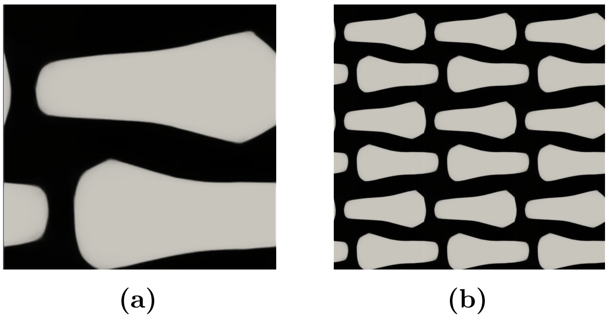

Figure 2.8: PANi + PCL (a) unit cell, (b) pattern.

In both cases, it can be noticed that the conductivity value was increased. This was due to the thickness of the struts that was increased, and it was generally a positive outcome since the purpose was to get a patch that substituted the role of the heart tissue in conducting current.

2.2.3 Mass minimization with modified constraints

An acceptable cell topology was found for five of the materials that were chosen from literature for their properties and compatibility with the heart tissue.

There were other materials with different mechanical and conductive properties that did not give any admissible solution neither with the objective function of mass minimization alone nor with mass minimization and E_{1111} minimization. This was due to a high value of the conductivity of the bulk material, that led to cell structures composed by very thin struts.

An example is a simulation run for a material composed of PANi, phytic acid and chitosan [40], that has bulk properties as follows:

$$E = 6.73\, MPa$$

$$k = 16.2\, S/m$$

Through mass minimization, the result of the simulation was a cell with the structure shown in Figure 2.3.

The struts of this cell were extremely thin with respect to the others that were obtained, and this may compromise the feasibility of the patch. Since the shape of the cell was promising, the same material properties were given as an input using mass and E_{1111} minimization, but no acceptable results were found. The requirements were met in some cases, but the structure turned out to be too complex.

These simulations were very sensitive to the properties of the bulk material, so it was possible that the Young's modulus of this material was too high and could not reach a well-defined structure and at the same time minimize E_{1111}. For this reason, it was decided to remove the objective function on E_{1111}, restoring a constraint on it with more restrictive values, which were:

$$0.01MPa < E_{1111} < 0.25MPa$$

These values were lower than the original ones and were chosen to force the code to minimize E_{1111} keeping the value of transverse stiffness E_1 acceptable (i.e. lower than 0.5 MPa).

The range of constraints for the conductivity was kept equal to five/ten times the one that was used for mass minimization alone.

The bulk properties of the materials under consideration that yielded satisfactory results are shown in Table 2.7.

Table 2.8 illustrates the constraints that led to a geometry in accordance with the specified requirements.

The homogeneous material properties were computed for each cell and are displayed in Table 2.9.

Figure 2.9, Figure 2.10, Figure 2.11, Figure 2.12 show cell structures and their corresponding patterns.

Table 2.7: Bulk properties of materials under consideration with modified constraints.

	E [MPa]	k [S/m]	ν
1-2. PANi + PCL + PGS [19]	1.3	6.3	0.4
3. Nanocellulose + PGS + PPy [1]	0.6	3.4	0.4
4. PANi + phytic acid + chitosan [40]	6.73	16.2	0.4

Table 2.8: Modified constraints for each material.

	E_{1111} [MPa]	E_{1122} [MPa]	E_{2222}/E_{1111}	k_{11} [S/m]	k_{22}/k_{11}
1.	$0.01 \div 0.25$	$-0.099 \div -0.015$	$0.3 \div 0.5$	$1.5 \div 4$	$0.35 \div 0.8$
2.	$0.01 \div 0.3$	$-0.101 \div -0.038$	$0.35 \div 0.5$	$1.5 \div 4$	$0.4 \div 0.8$
3.	$0.01 \div 0.25$	$-0.099 \div -0.015$	$0.3 \div 0.5$	$2.5 \div 4$	$0.35 \div 0.8$
4.	$0.01 \div 0.3$	$-0.099 \div -0.025$	$0.25 \div 0.5$	$4.1 \div 8$	$0.35 \div 0.8$

Table 2.9: Homogeneous properties of each material with modified constraints.

	E_1 [MPa]	Poisson	E_2/E_1	k_1 [S/m]	k_2/k_1
1.	0.25	-0.22	0.31	1.49	0.35
2.	0.20	-0.51	0.34	1.49	0.40
3.	0.17	-0.29	0.30	1.28	0.35
4.	0.29	-0.30	0.28	4.07	0.35

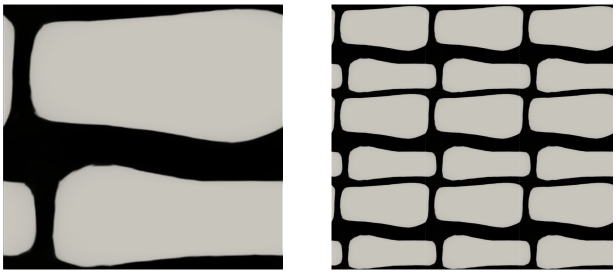

(a) **(b)**

Figure 2.9: PANi + PCL + PGS (1) (a) unit cell, (b) pattern.

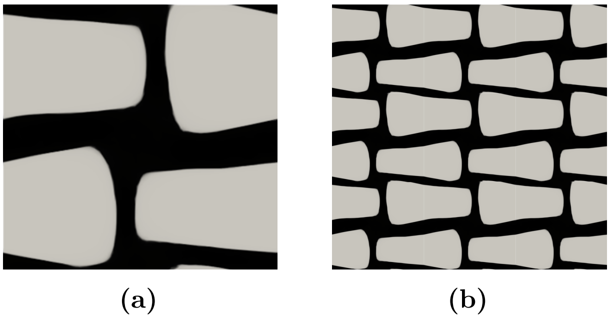
(a) (b)

Figure 2.10: PANi + PCL + PGS (2) (a) unit cell, (b) pattern.

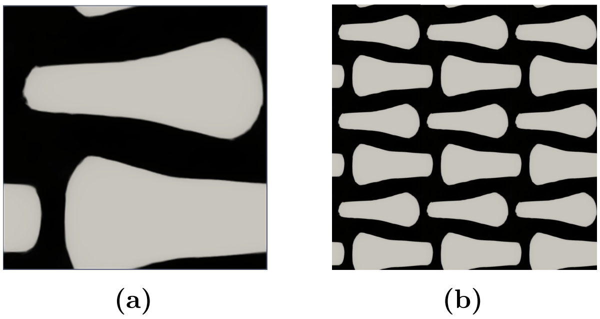
(a) (b)

Figure 2.11: Nanocellulose + PGS + PPy (a) unit cell, (b) pattern.

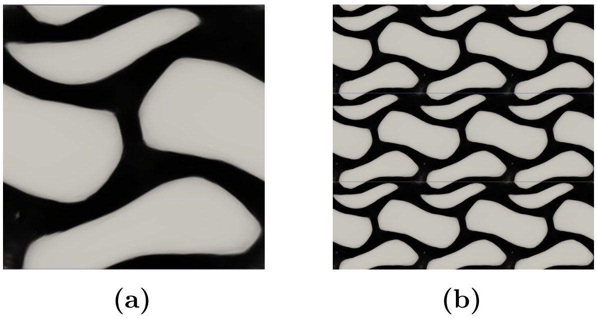
(a) (b)

Figure 2.12: PANi + phytic acid + chitosan (a) unit cell, (b) pattern.

2.3 Discussion

In section 2.2 one can find all cells whose mechanical and electrical characteristics fell within the ranges of cardiac tissue properties.

By visually comparing the obtained geometries, the most suitable structures from the feasibility point of view were those shown in Figure 2.8 and Figure 2.11, as they presented an enough simple pattern formed by thicker struts with respect to the other solutions.

The importance of strut thickness derives from the fact that a pattern with dimensions of 20 x 20 mm has cells with dimensions of 4 x 4 mm, considering, for example, five cells per side. Therefore, in the case of the two selected geometries, the struts had a thickness approaching one millimeter. Considering thinner struts would make their manufacture more demanding.

For the selected cells, an elastic and electrical simulation was made with *Abaqus* (Dessault Systèmes, 2019) to verify the consistency of results obtained in *FreeFEM*. This verification was done using a *Matlab* code (already developed in previous works) that took as an input the geometry of the cell in *.inp* format.

The values of the properties obtained with *Abaqus*, shown in Table 2.10 and Table 2.11, slightly differed from those resulting from the optimization code, and were therefore considered satisfactory.

Table 2.10: Properties of cell in Figure 2.8.

	E_1 [MPa]	Poisson	E_2/E_1	k_1 [S/m]	k_1/k_2
FreeFEM	0.60	-0.20	0.30	1.49	0.35
Abaqus	0.62	-0.21	0.31	1.57	0.36

Table 2.11: Properties of cell in Figure 2.11.

	E_1 [MPa]	Poisson	E_2/E_1	k_1 [S/m]	k_1/k_2
FreeFEM	0.17	-0.29	0.30	1.28	0.35
Abaqus	0.17	-0.32	0.30	1.33	0.47

Since the two cells were comparable, the first one was chosen to perform all the activities explained in the following chapters, keeping in mind that the entire procedure followed in this thesis can be declined for all the other solutions found.

Chapter 3

Morphological characterisation of the left ventricle from clinical images

In order to simulate the behaviour of the patch, both from a mechanical and conductive point of view, a model of heart tissue on which to apply the model of the patch must be generated. By analysing clinical images of cardiac computed tomography (CCT) the 3D model of a left ventricle is generated by segmenting the anatomy of the heart for a specific phase of the cardiac cycle. Once the model is obtained, it can be parameterized using a *Matlab* code that takes as an input the 3D model and a scale factor and gives as an output the 3D model scaled. The latter is used to simulate the deformation of the heart that occurs during a cardiac cycle as will be explained in chapter 4. Knowing the deformation of the heart tissue during a cardiac cycle is important to verify which conditions the patch needs to withstand.

3.1 Digital processing of clinical images

The reconstruction of the left ventricle involves the use of CCT images in DICOM format (Digital Imaging and COmmunications in Medicine, *.dicom*), provided by the research centre BioCardioLab of the Fondazione Toscana Gabriele Monasterio situated in Massa. They were acquired on a male patient of 82 years old. The data consisted in 10 sets of images, each of which represents the heart in a certain phase of the cardiac cycle. These images were originally used to study the morphology of the left atrium, therefore only one set out of ten includes the image of the entire left ventricle. This is the reason why there was no possibility of reconstructing the deformation of the heart tissue through the actual cardiac cycle images, but it was necessary to use a tool able to scale the model obtained by one single phase of the cycle.

The image set of interest was imported into *3D Slicer* and the images were processed using the segment editor function. First of all, an optimal segmentation threshold needed to be determined. From a qualitative point of view, it was possible to set the most suitable value of threshold by looking at the segmentations obtained in the sagittal, axial and frontal planes.

To understand the difference between the values of threshold, a comparison of three ranges is shown in Figure 3.1: 50-650, 150-650, 250-650. These ranges were only useful to get a first approximation of the final result and thus reduce the time for selecting the area of interest. The left ventricle was less subjected to the upper limit of the threshold because it had a white colour, but this limit was quite irrelevant to the result, so it was kept constant. The first threshold shown (50-650) better identified the pixels relative to the area of interest.

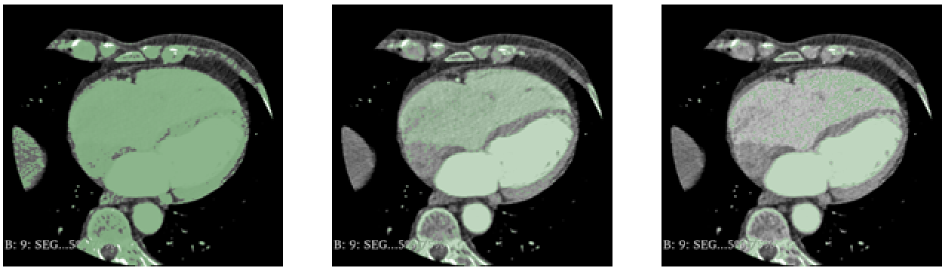

(a) 50-650 **(b)** 150-650 **(c)** 250-650

Figure 3.1: Comparison of the segmentation result with different thresholds in the axial view of *3D Slicer*.

After the selection of a suitable threshold, it was necessary to remove all the parts that were not coincident with the left ventricle. This was done in a first approximation, directly from the 3D reconstruction of the slices. When all the redundant parts were deleted, a more accurate removal of segmentation was performed.

The segmented ventricle was exported in STL format (i.e., STereo Lithography, *.stl*), which represents a discretized shell. Subsequently, the files were imported into *Autodesk Meshmixer* (Autodesk, California, USA), a free software used for the post-processing of 3D models that need optimisation of shape or remeshing. This step was necessary because, following segmentation, the ventricle model had several imperfections and presented a very jagged surface. This problem was solved using some filters to smooth out irregularities in the surface. Once the surface was qualitatively improved, the model was exported again using STL format.

Figure 3.2 shows the result of the post-processing operations step by step: segmentation, post processing in *3D Slicer*, post processing in *Meshmixer*.

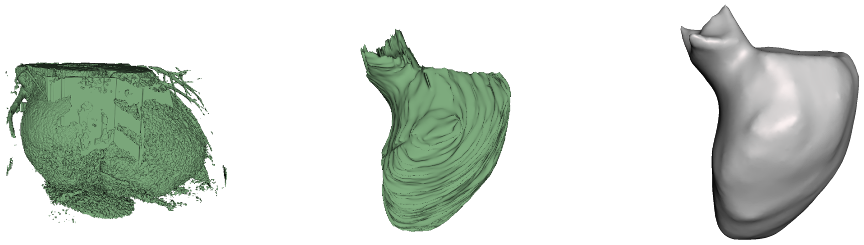

(a) **(b)** **(c)**

Figure 3.2: Post-processing operations to obtain the ventricle model: (a) Thresholding (b) *3D Slicer* (c) *Meshmixer*.

In order to create a likely model of the heart, both the cavity of the left ventricle and the tissue of the ventricle must be considered. Therefore, with the same methodology that is described in this paragraph, two STL models were generated: one was representative of the ventricular cavity, the other represented the ventricle including all the tissue until its external wall. Using *HyperMesh* (Altair HyperWorks, USA), the two shells were combined together (one inside the other) to create a solid wall filling the gap between them and incorporating a cavity (Figure 3.3).

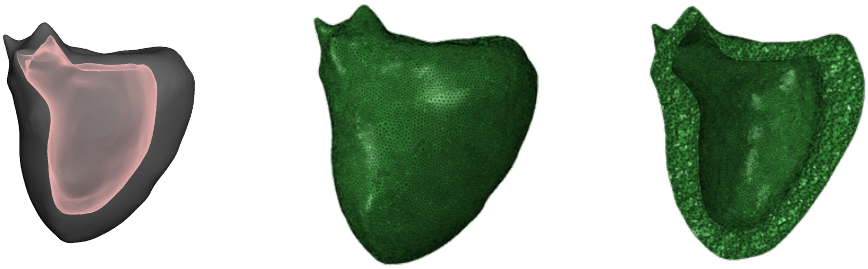

(a) **(b)** **(c)**

Figure 3.3: Construction of a solid model of the ventricle: (a) External and internal shells. (b) Complete model (c) Section of the model.

3.2 Post processing of left ventricle model

The reproduction of the heart tissue deformation during the cardiac cycle was performed to verify the entity of the deformation of the patch once it was applied to the tissue. Since it was not possible to obtain all the instants of the cardiac cycle from the heart segmentations, as explained in section 3.1, another method needed to be found to reproduce a plausible simulation of the swelling of the heart from a single model.

The idea was to derive from the model some typical measurements of the ventricle, such as the volume of the ventricular cavity, the length between the apex of the cavity and the mitral valve, and the area of the mitral valve itself. Although it was not precisely known what phase of the cycle the model corresponds to, it was known that it was in an intermediate phase between the end of systole and the end of diastole, as shown on a previous study on the same clinical images [25]. Thus, data regarding the above measurements in the phases of end-systole and end-diastole were searched in literature, for different samples of patients, to find one or more samples such that the measurements of the reconstructed model fall within their range.

To evaluate the characteristic parameters of the ventricle from the model, different software were used.

For the volume, *Autodesk Meshmixer* simply allowed to import the STL model and look for the volume inside the shell model. What was found is:

$$V_{i,i} \cong 165\, ml$$

$$V_{i,e} \cong 296\, ml$$

Where $V_{i,i}$ is the volume of the internal cavity of the ventricle in the intermediate phase of the cycle, while $V_{i,e}$ is the volume of the ventricle in the same phase of the cycle comprising both the cavity and the ventricle tissue. Assuming that the volume of the heart tissue remained constant during the cardiac cycle, it was possible to derive its value, that will be useful for the total volume:

$$V_{i,t} = V_{i,e} - V_{i,i} \cong 131\, ml$$

Autodesk Meshmixer was used also for the evaluation of the length l of the ventricle, that was found to be:

$$l \cong 76\, mm$$

To evaluate the area A of the mitral valve, *3-matic* (Materialise, Leuven, Belgium, 2022) was used (Figure 3.4), by selecting an approximate area of the mitral valve based on anatomical images (Figure 3.5). This measure was probably not very accurate, but a possible value was:

$$A \cong 12.8\,mm^2$$

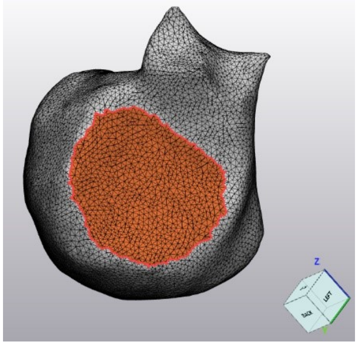

Figure 3.4: Mitral valve highlighted (in orange) on ventricle model using *Materialise 3-matic.*

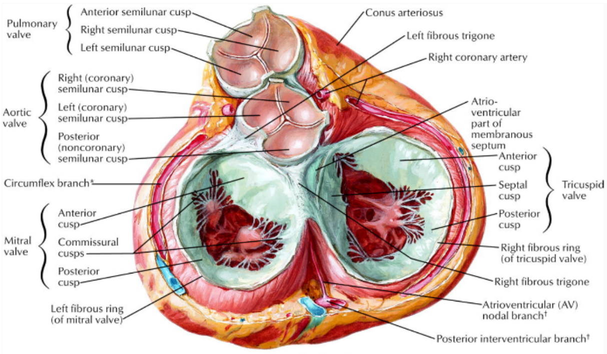
Pulmonary valve
Anterior semilunar cusp
Right semilunar cusp
Left semilunar cusp
Aortic valve
Right (coronary) semilunar cusp
Left (coronary) semilunar cusp
Posterior (noncoronary) semilunar cusp
Circumflex branch*
Mitral valve
Anterior cusp
Commissural cusps
Posterior cusp
Left fibrous ring (of mitral valve)
Conus arteriosus
Left fibrous trigone
Right coronary artery
Atrio-ventricular part of membranous septum
Anterior cusp
Septal cusp
Posterior cusp
Tricuspid valve
Right fibrous ring (of tricuspid valve)
Right fibrous trigone
Atrioventricular (AV) nodal branch†
Posterior interventricular branch†

Figure 3.5: Heart in diastole: view from base with atria removed [17].

A large number of studies concerning healthy ventricle measures were found [3, 11, 15, 35, 39, 42–46, 48, 50–52, 55–57, 59, 62, 68], but no one had information about all the three parameters together. Also, the value of the mitral valve area was not coherent and thus could not be used. Moreover, all the studies that give information about the ventricular cavity length did not mention any measure of the volume.

Therefore, it was decided to focus the attention only on one parameter, the one with more data available, that in this case was the volume of the ventricular cavity. Since the value of interest was 165 ml, a possible range that had this value as an intermediate value was found in a study concerning 20 healthy male subjects [11] for whom the volume of the ventricular cavity at end-diastole and end-systole was calculated, obtaining:

$$V_{e,d} = 181.1 \pm 30.3\, ml$$

$$V_{e,s} = 70.7 \pm 18\, ml$$

Where $V_{e,d}$ is the volume at end-diastole and $V_{e,s}$ is the volume at end-systole. For all the other studies, these values were too small, and the volume of interest did not fall within the results.

A new model of the ventricle was then created, scaling the original one till it reached a value of the volume more or less equal to $V_{e,s}$. Then, a pressurization test was done to see if, applying a physiological pressure on the internal wall of the ventricle, the value $V_{e,d}$ was reached.

To scale the model, a *Matlab* code was used, that took as an input a scale factor and the 3D model with *.inp* format and gave as an output the 3D model scaled with the same format. The scale factor was not known, so a procedure of trial and error was done, starting with a random value, and then measuring the volume of the model obtained using *Autodesk Meshmixer*. The value of the scale factor was regulated until the volume of the ventricle reached approximately $V_{e,s}$.

To obtain the model of the external wall of the ventricle in the end-systolic phase, the same procedure was used, knowing that the volume that has to be reached was $V_{e,s} + V_{i,t}$, since it was supposed that the volume of the tissue did not change. At the end, the correct values of volume were approximately reached, using as scales factor for the internal cavity volume and the external wall volume respectively 0.75 and 0.88. The result is shown in Figure 3.6.

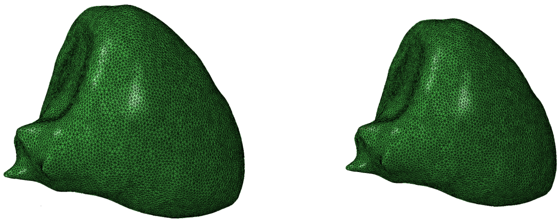

(a) **(b)**

Figure 3.6: Scaling of the ventricle with cavity volume equal to (a) 165 ml (b) 70 ml.

Chapter 4

Cardiac cycle simulation with pressurization tests

Once obtained the model of the ventricle at end-systole, i.e. in the phase when it is most contracted, the purpose was to simulate the filling of the ventricle due to the inflow of blood, in order to evaluate the deformations that the heart tissue and the patch are subjected to.

Before running simulations on the model obtained in chapter 3, two simplified models (i.e. a parallelepiped and an ellipsoid) were used to assess the most suitable material to be used and the parameters to be associated with it.

4.1 Tests on parallelepiped

4.1.1 Model design

To identify the most appropriate material for mimicking cardiac tissue mechanics, initial simulations were conducted on a simplified geometry for rapid and straightforward interpretation.

Using *Abaqus*, the model was designed with a parallelepiped-shaped geometry. The infarcted region was modeled as a smaller parallelepiped obtained in the centre (Figure 4.1). This arrangement allowed to assign a distinct material to the infarct, characterized by higher stiffness [16, 23]. The dimensions of the parallelepiped were 120 x 60 x 10 mm, the ones of the infarcted region were 10 x 10 x 10 mm.

To evaluate the potential advantage of using an auxetic patch, an initial simulation was performed with a solid rectangular-shaped patch (Figure 4.2), followed by one using the actual patch geometry (Figure 4.3).

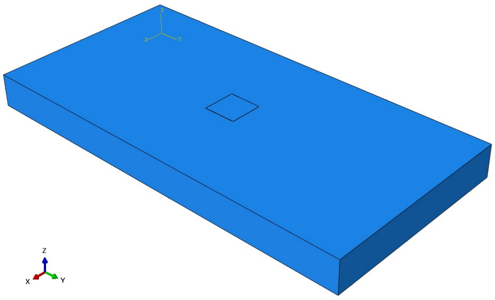

Figure 4.1: Simplified representation of heart tissue and infarct with a parallelepiped-shaped geometry.

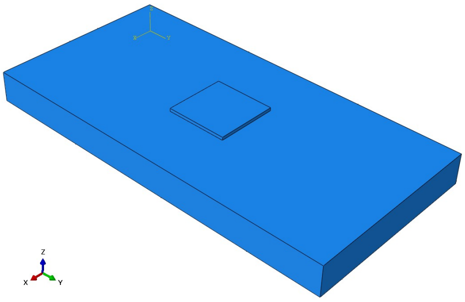

Figure 4.2: Simplified model of heart tissue and rectangular-shaped patch.

As shown in Figure 4.2 and Figure 4.3, in both cases the patch was positioned at the centre of the upper surface of the heart model and adherent to it with dimensions equal to 20 x 20 x 1 mm.

Creating the fully-solid patch as a component in *Abaqus* was straightforward. The process was different for the auxetic patch, because the optimization tool that generated its geometry did not provide a CAD file, but rather supplied a file in *.vtk* format showing the material density distribution of the cell. This file was first imported in *ParaView* (an open source visualization application maintained by Kitware, Inc.) for post-processing. The density distribution of the cell had intermediate values comprised between zero and one, especially at the edges of the struts. For this reason, it was necessary to apply a filter to discriminate the solid part from the void part of the cell, setting a minimum density value below which the solid material was not considered. Then, the cell surface was constructed and a triangular mesh was created, so that the file could be exported in *.stl* format and used to render the three-dimensional geometry.

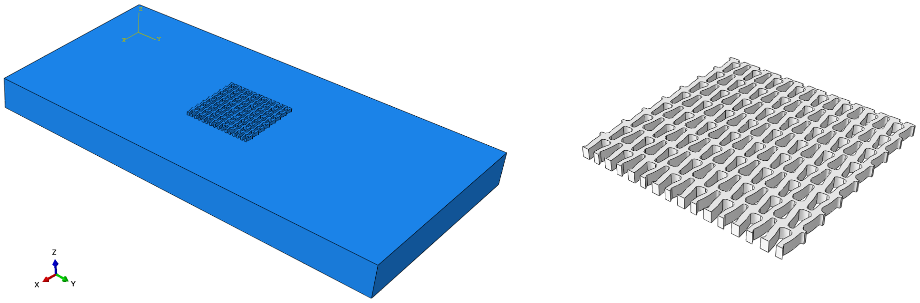

(a) **(b)**

Figure 4.3: Parallelepiped-shaped model of heart tissue with auxetic patch. (a) Complete model. (b) Enlargement of patch.

The cell in *.stl* format measured 1 x 1 mm, which was why it was imported in *3-matic* and scaled in order to obtain a dimension of 2.5 x 2.5 mm, so that, with eight cells per side, the desired patch size (i.e. 20 x 20 mm) was achieved.

Then, it was imported in *Abaqus* and a surface was created from the mesh elements, a rectangular pattern with eight cells per side was made and finally the surface was extruded of 1 mm.

4.1.2 Materials and boundary conditions

Materials

There are several material models in literature aimed at describing the mechanical behavior of cardiac tissue [4, 18, 36, 69]. Due to their complexity, these models are well-suited for uncomplicated geometries.

It was chosen to use Fung's model [4] as it has already been implemented, through its strain energy function, in *Abaqus* among orthotropic hyperelastic materials.

The exponential constitutive law presented in Equation 4.1 demonstrates a transversally isotropic material behavior which differs in the fibre direction compared to the two orthogonal directions, where the response remains consistent.

$$W = \frac{1}{2}C\left(e^{b_1 e_{ff}^2 + b_2\left(e_{rr}^2 + e_{ss}^2 + 2e_{sr}e_{rs}\right) + 2b_3\left(e_{fs}e_{sf} + e_{fr}e_{rf}\right)} - 1\right) \tag{4.1}$$

The subscript f refers to the local fibre direction, while r and s are the radial and cross-fibre direction, respectively. The parameters C, b_1, b_2, b_3 were experimentally derived with tests on pig hearts [4]. They were entered as input in *Abaqus* consistently with the fibre arrangement corresponding to direction 1. The values of these parameters are reported in Table 4.1.

Table 4.1: Experimentally derived material constants for Fung's model.

C [MPa]	b_1	b_2	b_3
$6.95 \cdot 10^{-5}$	83.43	36.37	62.36

The incompressibility hypothesis was established through a parameter (i.e., D in *Abaqus*) imposed equal to zero.

The auxeticity of Fung's model was achieved through the arrangement of a certain number of layers, each with a different fibre orientation. As it will be shown in subsection 4.1.3, the auxetic behavior was not achievable using the same fibre orientation for all layers.

For the present case, it was decided to divide the parallelepiped-shaped model into four layers, following what is suggested in literature [4] and using *Abaqus*. The individual layers, each 2.5 mm thick, were associated to a local reference system. Here, direction 1 aligned with a particular fibre orientation visually represented in Figure 4.4 and detailed in Table 4.2.

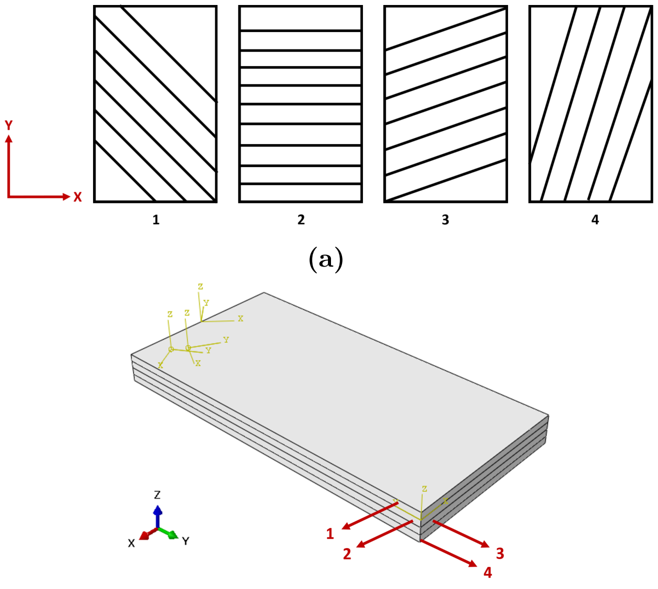

(a)

(b)

Figure 4.4: Representation of the partition of the model into four layers. (a) Schematic representation of the four layers and (b) three-dimensional model.

Table 4.2: Angle of fibre orientation with respect to x-direction.

Layer 1	Layer 2	Layer 3	Layer 4
135°	0°	30°	60°

For both the infarcted region and the patch a linear elastic material was imposed. For the former, the Young's modulus was configured to be tenfold higher than the value documented in literature for healthy heart tissue [16, 23], effectively emulating a more rigid region. For the latter, the bulk properties of the material selected in section 2.3 were used. The values required by *Abaqus* are summarized in Table 4.3, assuming the incompressibility of the materials.

Table 4.3: Properties of the linear elastic materials used for infarcted region and patch.

	Young's modulus [MPa]	Poisson's ratio
Infarcted tissue	0.5	0.47
Patch	2	0.4

The mesh of all parts had tetrahedral elements and their average size is reported in Table 4.4.

Table 4.4: Average size of mesh elements for the different parts of the parallelepiped-shaped model.

Healthy heart tissue	Infarcted region	Simplified patch	Auxetic patch
1.5 mm	1.5 mm	0.5 mm	0.19 mm

Boundary conditions

Between the different parts, in the contact regions, a constraint of type *Tie* was set in *Abaqus*.

The load imposed on the parallelepiped consisted of a displacement in the y-direction equal to 10% of the total length and exerted on the face highlighted in red in Figure 4.5. The boundary conditions were applied to the face opposing to the loading one and consisted of a zero displacement in the y-direction. An edge of the same face was encastred to avoid excessive edge effects that would result from constraining the entire face in all three directions.

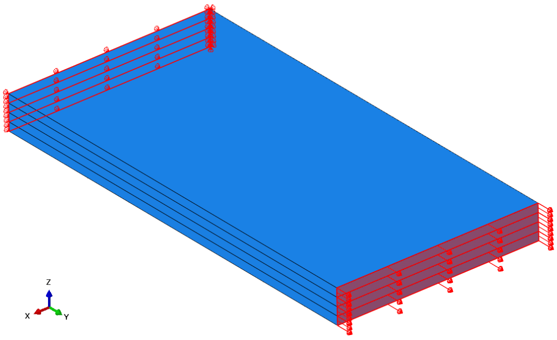

Figure 4.5: Load and boundary conditions applied to the parallelepiped-shaped model.

4.1.3 Results and discussion

To confirm the auxeticity of Fung's model, a mechanical simulation was conducted using a simplified parallelepiped structure arranged in layered configuration with varying fibre orientations, as explained in subsection 4.1.2.

When a load in y-direction is imposed, Poisson's ratio ν is defined as

$$\nu = -\frac{\varepsilon_x}{\varepsilon_y} \tag{4.2}$$

where ε_x and ε_y are the deformations in x- and y-direction, respectively. These values were computed considering two points situated at the ends of each pair of opposing sides, as illustrated in Figure 4.6, for different levels of the model thickness (i.e., every 1.25 mm from z = 0 mm to z = 10 mm), and the following equations were applied to determine the deformations:

$$\varepsilon_x = \frac{U_{x1} - U_{x2}}{L_{x0}} \tag{4.3}$$

$$\varepsilon_y = \frac{U_{y3} - U_{y4}}{L_{y0}} \tag{4.4}$$

where U_{x1} and U_{x2} are the displacements in the x-direction of the two points in Figure 4.6a, while U_{y3} and U_{y4} are the displacements in y-direction of the two points in Figure 4.6b. L_{x0} and L_{y0} are the initial distances between the points in their respective directions.

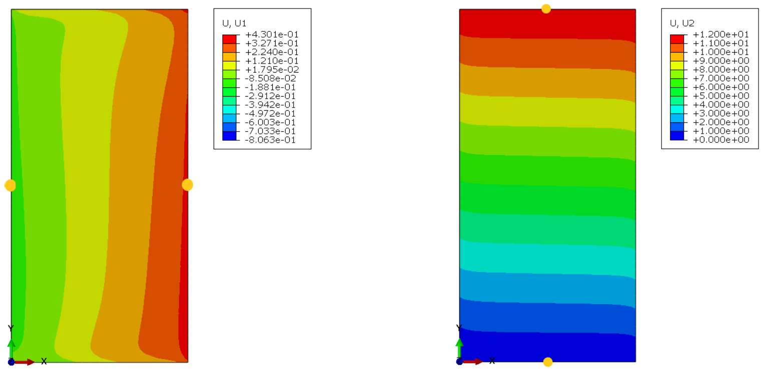

(a) **(b)**

Figure 4.6: Selection of the points located on the top surface (i.e., z = 10 mm) to verify the auxeticity of Fung's model. (a) Displacement field in x-direction. Point 1 on the right, point 2 on the left. (b) Displacement field in y-direction. Point 3 on the top, point 4 on the bottom.

The value of Poisson's ratio was obtained considering the mean value of the deformations in the thickness, obtaining -0.02, meaning this model was indeed exhibiting an auxetic behaviour.

To demonstrate that achieving the same result was not possible without this arrangement of the layers, a mechanical simulation was performed on a model with equally oriented fibres. The same parameters were extracted, as previously described, resulting in a Poisson's ratio value of 0.26.

Simulations including an infarted region and a patch were then performed to enable a comparative analysis of the deformation state of cardiac tissue across four distinct cases: healthy tissue, tissue with infarction, damaged tissue with the incorporation of a rectangular or an auxetic patch.

Initially, a verification of the behavior of both patch designs was conducted by computing their Poisson's coefficient. The same formulas applied to the parallelepiped were used for these calculations. The resulting values demonstrated that the patch with the patterned configuration exhibited auxetic performance characterized by $\nu = -0.004$, in contrast to the rectangular patch that had $\nu = 0.32$.

To analyse the deformation field of the cardiac tissue, two paths aligned with x- and y-direction were created for each layer at half of their thickness. In Figure 4.7 only the paths on the superficial layer are shown as an example.

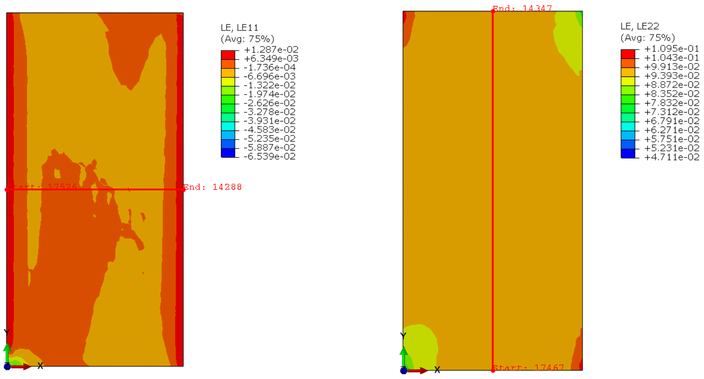

(a) (b)

Figure 4.7: Selection of two paths in the superficial layer to evaluate deformations in the heart tissue. (a) Strain field in transverse direction. (b) Strain field in longitudinal direction.

The acquired data, depicted in the graphs in Figure 4.8, demonstrated the inevitable impact of the infarct on the deformation field of cardiac tissue due to its higher stiffness. The influence of an auxetic patch was comparable to the one of the rectangular patch. However, the deformations of the heart tissue in the presence of a patterned device were closer to those observed in the infarcted ventricle. Outside the patch region, strain values converged towards cardiac tissue levels.

Given the layered structure of the model characterized by an asymmetrical fibre orientation, the imposed displacement caused not only traction but also slight bending. This effect was more pronounced in the upper and lower layers. Regarding longitudinal deformations (i.e., analogous to the circumferential ones in the heart), the first layer experienced a greater impact from the patch application since it was the layer directly beneath it. Comparing the case with infarction and the ones with the application of the patch, the fourth layer exhibited no discernible difference in terms of deformation. In the two intermediate layers, the presence of the device was capable of redistributing mechanical overstress and reducing by approximately 16% the peaks of deformation caused by the infarct, which behaved like a hard inclusion embedded within healthy tissue.

Regarding transverse deformations (i.e., analogous to the axial ones in the heart), their magnitude, equal to approximately 1%, was lower than that of longitudinal strains. Consequently, even with the presence of the patch, which slightly modified the range of deformations compared to an infarcted heart, the situation did not worsen.

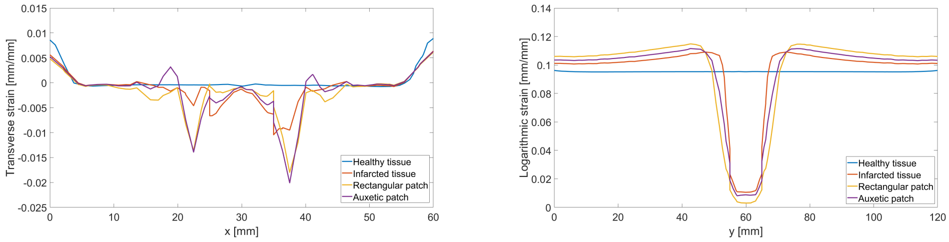

(a) Layer 1 **(b)** Layer 1

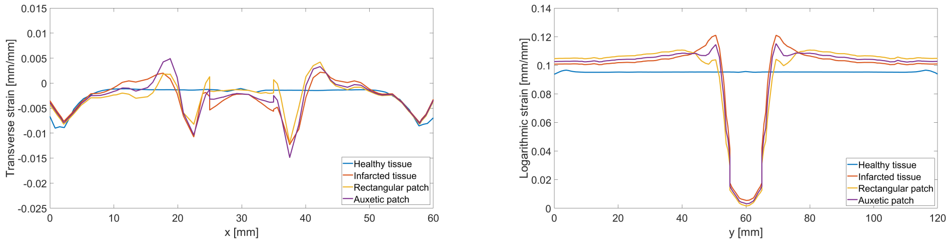

(c) Layer 2 **(d)** Layer 2

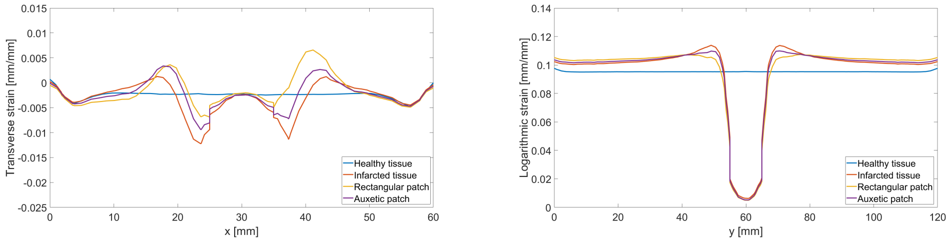

(e) Layer 3 **(f)** Layer 3

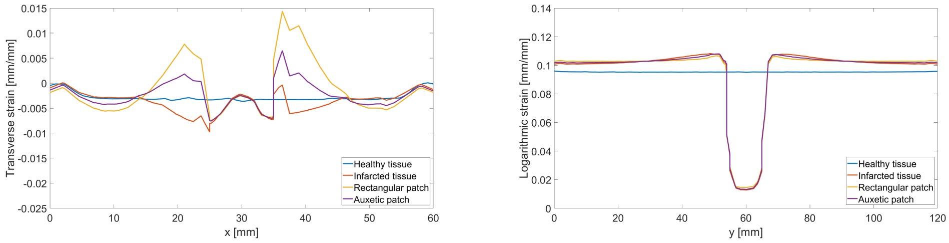

(g) Layer 4 **(h)** Layer 4

Figure 4.8: Deformation of the heart tissue in (a), (c), (e), (g) x-direction, (b), (d), (f), (h) y-direction.

The graph in Figure 4.9 compares the maximum deformation value in the longitudinal direction for the infarcted ventricle with and without the auxetic patch. In presence of the device, this strain decreased in all the layers, with the exception of the first one, which, being positioned directly beneath the patch, was most affected.

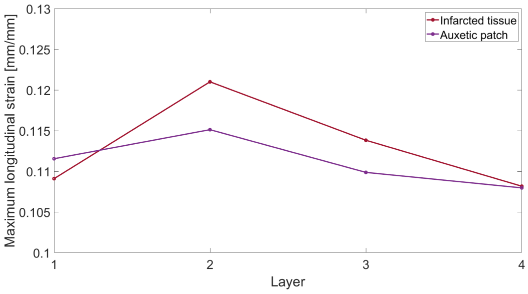

Figure 4.9: Maximum longitudinal strain for each layer evaluated for infarcted ventricle with and without auxetic patch.

4.2 Tests on semi-ellipsoid

4.2.1 Model design

After choosing the Fung's material to replicate heart tissue properties, the geometry of the model was refined to closely resemble that of the heart, while still maintaining simplicity.

An *Abaqus* model was constructed, representing a hollow semi-ellipsoid designed to mirror the left ventricle. In order to simulate the infarcted region, a circular hole was initially generated within the ellipsoid wall. Subsequently, this void was replaced with a geometric component that matched the surrounding structure, differentiating it from the adjacent healthy cardiac tissue with distinct properties. The model is shown in Figure 4.10.

As explained in subsection 4.1.1, the optimization tool that generated the geometry of the patch did not provide a CAD file, but rather supplied a file in *.vtk* format showing the material density distribution of the cell. Using *Paraview* and *3-matic* and following the same procedure described in subsection 4.1.1, a two-dimensional planar cell was obtained and imported in *Abaqus*. A pattern was generated using five cells per side and it was saved as a sketch. Following this, a plane tangential to the ellipsoid was created in the region of the infarct and onto it the previously crafted sketch was imported, enabling the creation of an extruded cut. This procedure produced a two-dimensional patch following the ellipsoid curvature. Subsequently, *3-matic* was employed to establish the patch thickness (i.e., 1 mm) and the mesh, with tetrahedral elements of average size of 0.1 mm. The final outcome was reintegrated into the *Abaqus* environment, obtaining the model shown in Figure 4.11.

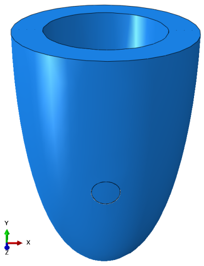

Figure 4.10: Simplified representation of the infarcted ventricle using a hollow semi-ellipsoid. Wall thickness: 10 mm, height: 85 mm, radius of internal upper circumference: 20 mm.

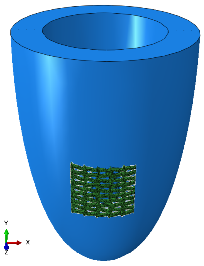

Figure 4.11: Hollow semi-ellipsoid with a patch that follows its curvature.

4.2.2 Materials and boundary conditions

Materials

To establish four layers and enable the assignment of distinct fibre orientations to each of them, as outlined in Fung's model, the *Abaqus* part was partitioned into four hollow semi-ellipsoids with thickness equal to 2.5 mm, as shown in Figure 4.12.

The infarcted ventricle model was meshed with tetrahedral elements measuring 2.5 mm, on average.

In this scenario, unlike the case of a parallelepiped geometry, assigning a singular local reference system to each layer was unfeasible due to the model curvature. For highest accuracy, the optimal approach allocates a distinct local reference system to each element of the mesh, based on both its angular position and the layer it belongs to. Given the clear impracticality of this procedure, a *Matlab* code was developed to systematically divide each layer into 10° wide circular sectors (Figure 4.13) and to assign the pertinent reference system to each of these portions. To effectively segment the mesh elements, a shift from Cartesian coordinates to polar coordinates was necessary. Then, a rotation matrix was used to assign the corresponding reference system to each sector, taking into account both its angular position and the orientation angle of the fibres within each layer.

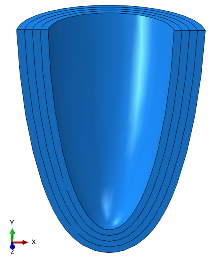

Figure 4.12: Longitudinal section of the hollow semi-ellipsoid partitioned in four layers.

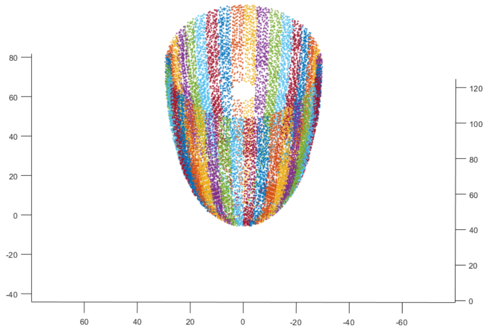

Figure 4.13: Segmentation of one layer of the healthy tissue into 10° wide portions using *Matlab*.

The parameters of Fung's model and the material properties for the infarcted region and the patch were those reported in subsection 4.1.2.

Boundary conditions

Between the different parts, in the contact regions, a constraint of type *Tie* was set in *Abaqus*.

The applied load consisted of a pressure equal to 40 mmHg (i.e., 0.0053 MPa), exerted on the inner surface of the ellipsoid, following a ramp function. This simulation mirrored the physiological condition present within the left ventricle. The imposed value was the difference between the average maximum arterial pressure of 120 mmHg and the minimum of 80 mmHg. The simulation lasted for one second, i.e., the duration of a single heartbeat.

Boundary conditions were established by restricting the displacement of the upper circular crown along all three directions, as shown in Figure 4.14.

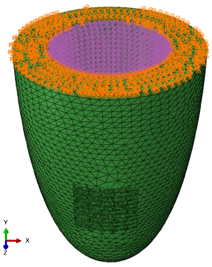

Figure 4.14: Load and boundary conditions applied to the ellipsoidal model.

4.2.3 Results and discussion

Volume variation

Simulations were conducted to reproduce as far as possible the deformation cardiac tissue undergoes during the cardiac cycle, particularly in terms of variation of cavity volume.

Referring to the numerous studies that have assessed left ventricular cavity size at the end of systole and the end of diastole [3, 11, 15, 35, 39, 42–46, 48, 50–52, 55–57, 59, 62, 68], on average, the volume variation experienced by the cavity during the cardiac cycle is 70 ml. This value is indicative and can exhibit significant variability, as it is derived from the difference between average volume measurements at the end of systole and the end of diastole, both of which possess substantial standard deviations, typically on the order of tens of millilitres.

The simulation involved the ellipsoidal model of healthy tissue, to which an internal pressure was applied, as outlined in subsection 4.2.2.

Starting from a cavity volume of 62 ml, calculated using *Meshmixer*, a volume of 90.7 ml was reached, and thus, there was a volume change of

28.7 ml. A visual representation of the outcome is found in Figure 4.15.

(a) t = 0 s

(b) t = 1 s

Figure 4.15: Pressurization test on ellipsoidal model at initial and final instants, with internal pressures equal to (a) 0 mmHg, and (b) 40 mmHg.

The same simulation was also conducted on both the simplified ellipsoidal model with infarcted tissue and the model with the patch, that were illustrated in subsection 4.2.2, obtaining approximately the same result in terms of variation in cavity volume.

The way Fung material was modelled in this work revealed some limitations, as it failed to predict the expected volume variation. This discrepancy might arise from approximations made in modelling the layers. Specifically, the reference systems established for each 10° wide circular sector, which varied between layers, may not accurately reflect the orientation of the fibres in the apex of the heart, where curvature is more pronounced.

Deformation field on cardiac tissue

A comparative analysis was conducted to evaluate the strains on cardiac tissue during a simulated heartbeat across three distinct cases: healthy tissue, tissue with infarction, and damaged tissue with the application of an auxetic patch.

From the results of the pressurization tests detailed in the previous paragraph, longitudinal and circumferential deformations were extracted along two paths situated near the patch, as illustrated in Figure 4.16. To achieve this, a cylindrical reference system was established within the *Abaqus* results environment, with the three directions ordered as radial, circumferential, and axial.

The acquired data are depicted in the graphs in Figure 4.17 and demonstrated the inevitable impact of the infarct on the deformation field of cardiac tissue. The presence of the infarcted region reduced by approximately

70% the value of deformations in the damaged area, due to its increased stiffness. Nevertheless, in the surrounding tissue, the percentage of this strain variation lowered. Notably, the introduction of the patch did not have a negative impact, as indicated by the similarity in strain trends between infarcted tissue with and without the patch. This outcome was predictable, as it had already been achieved in the simplified model.

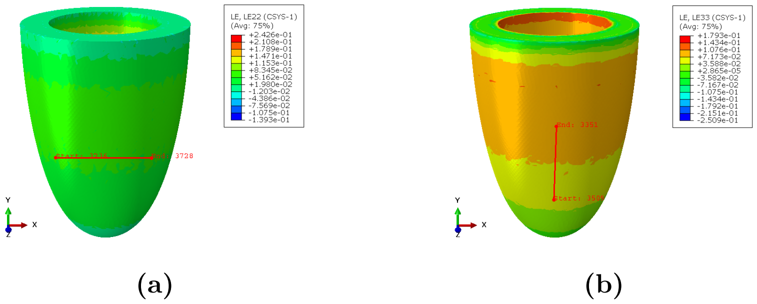
LE, LE22 (CSYS-1)
(Avg: 75%)
+2.426e-01
+2.108e-01
+1.789e-01
+1.471e-01
+1.153e-01
+8.345e-02
+5.162e-02
+1.980e-02
-1.203e-02
-4.386e-02
-7.569e-02
-1.075e-01
-1.393e-01
LE, LE33 (CSYS-1)
(Avg: 75%)
+1.793e-01
+1.434e-01
+1.076e-01
+7.173e-02
+3.588e-02
+2.865e-05
-3.582e-02
-7.167e-02
-1.075e-01
-1.434e-01
-1.792e-01
-2.151e-01
-2.509e-01
Y
X
Z

(a) **(b)**

Figure 4.16: Selection of two paths to evaluate deformations in the ellipsoidal model. (a) Strain field in circumferential direction, (b) Strain field in axial direction.

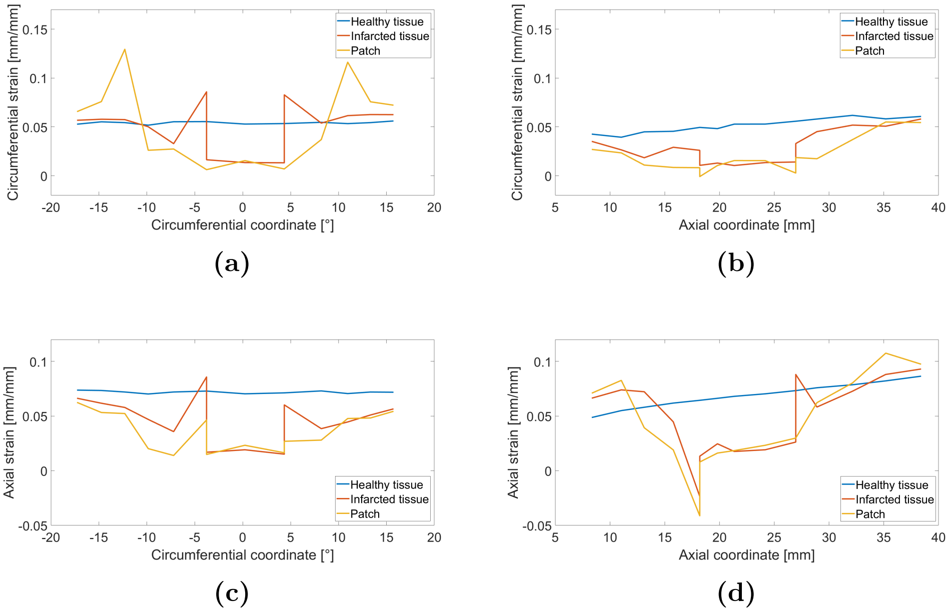

(a) **(b)**

(c) **(d)**

Figure 4.17: Circumferential strain of the ellipsoidal model in (a) circumferential direction, (b) axial direction. Axial strain in (c) circumferential direction and (d) axial direction.

4.3 Tests on realistic left ventricle

4.3.1 Model design

Although the auxetic material obtained with Fung's model cannot be easily used on complex designs, some simulations were nevertheless conducted on the realistic ventricle model described in chapter 3, using a more manageable material.

Through *Abaqus*, the left ventricle was meshed with tetrahedral elements having an average side length of 1.5 mm. Then, it was modified by adding the damaged region, in particular a set of elements corresponding to the infarct was created and converted into a part. In this way, two distinct parts were obtained, one for healthy tissue and one for damaged tissue, and different mechanical characteristics could be assigned.

In the region above the infarct, a patch that adapted to the curvature of the heart was obtained, following the same procedure described in section 4.2. The mesh elements of this part measured 0.1 mm on average.

The model with and without the patch is shown in Figure 4.18.

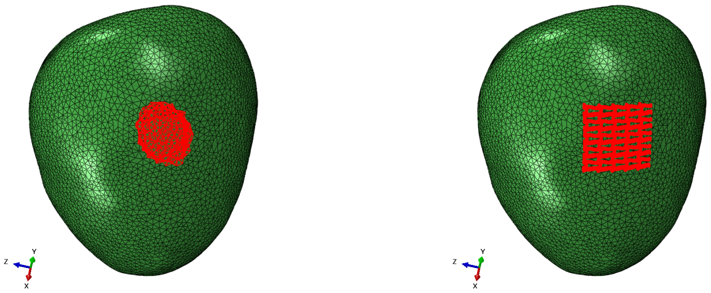

(a) **(b)**

Figure 4.18: Model of left ventricle with (a) an infarcted region and (b) a patch above it.

4.3.2 Materials and boundary conditions

Materials

The hyperelastic Neo-Hookean material was chosen as the simplest material approximating the behaviour of the heart, even if it does not truly represent it, being it isotropic.

However, it stands as the most straightforward hyperelastic material already implemented in *Abaqus* and its coefficients are derived from well-known properties, i.e., Young's modulus and Poisson's ratio. In contrast, other material models demand parameters that are not available.

Equation 4.5 shows the strain energy per unit reference volume characterising this material model.

$$W = C_{10}\left(\overline{I_1} - 3\right) + \frac{1}{D}\left(J_{el} - 1\right)^2 \tag{4.5}$$

C_{10} and D are temperature-dependent material parameters, and $\overline{I_1}$ is the first deviatoric strain invariant. The parameter D was set equal to zero. In this way, *Abaqus* established the incompressibility hypothesis. The expression for C_{10} is defined in Equation 4.6.

$$C_{10} = \frac{\mu_0}{2} \tag{4.6}$$

where

$$\mu_0 = \frac{E_0}{2\left(1 + \nu\right)} \tag{4.7}$$

and E_0 is the initial Young's modulus of the material, while ν is its Poisson's ratio. The imposed values were $E_0 = 0.05$ MPa and $\nu = 0.47$.

The material properties for the infarcted region and the patch were the same as the ones reported in subsection 4.1.2.

Boundary conditions

Between the different parts, in the contact regions, a constraint of type *Tie* was set in *Abaqus*. The applied load consisted of a pressure equal to 40 mmHg (i.e., 0.0053 MPa), as it was set for the ellipsoidal model, exerted on the inner wall of the ventricle. Boundary conditions were established by restricting the displacement of the mitral valve area and the aorta along all three directions, as shown in Figure 4.19.

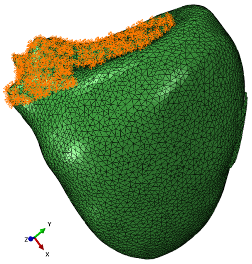

Figure 4.19: Boundary conditions applied to the ventricle model.

4.3.3 Results and discussion

Before applying the Neo-Hookean material to the more complex ventricle model, a preliminary test was conducted on the ellipsoid. The test replicated the conditions described in section 4.2, changing only the material used. The pressurization test resulted in an end-diastole cavity volume of 112 ml (Figure 4.20), meaning a variation of 50 ml with respect to end-systolic volume (i.e., 62 ml). This value was more closely aligned with physiological conditions compared to the one obtained with the Fung's model.

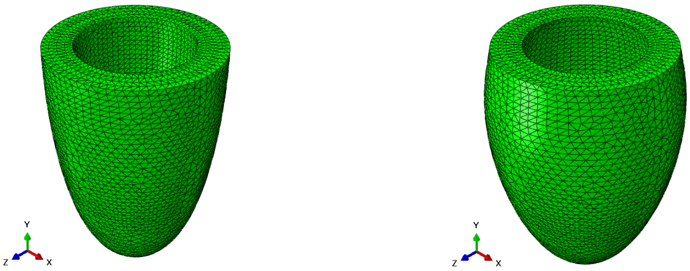

(a) t = 0 s **(b)** t = 1 s

Figure 4.20: Pressurization test on Neo-Hookean ellipsoidal model at initial and final instants, with internal pressures equal to (a) 0 mmHg, and (b) 40 mmHg.

Regarding deformations, the same strain values described in subsection 4.2.3 were extracted from this test, revealing a distinct behavior between the Neo-Hooke material and the Fung one, as shown in Figure 4.21. This outcome was expected, due to the isotropic nature of the former and the auxetic properties of the latter.

Nonetheless, it was decided that the Neo-Hooke material would be employed for the ventricle model, aiming to evaluate both the entity of volume variation and the deformations it underwent.

The pressurization test resulted in an end-diastole cavity volume of 116.3 ml (Figure 4.22), meaning a variation of 46.3 ml with respect to end-systolic volume (i.e., 70 ml). This value was in accordance with data found in literature regarding physiological volume variations of the left ventricle during the cardiac cycle.

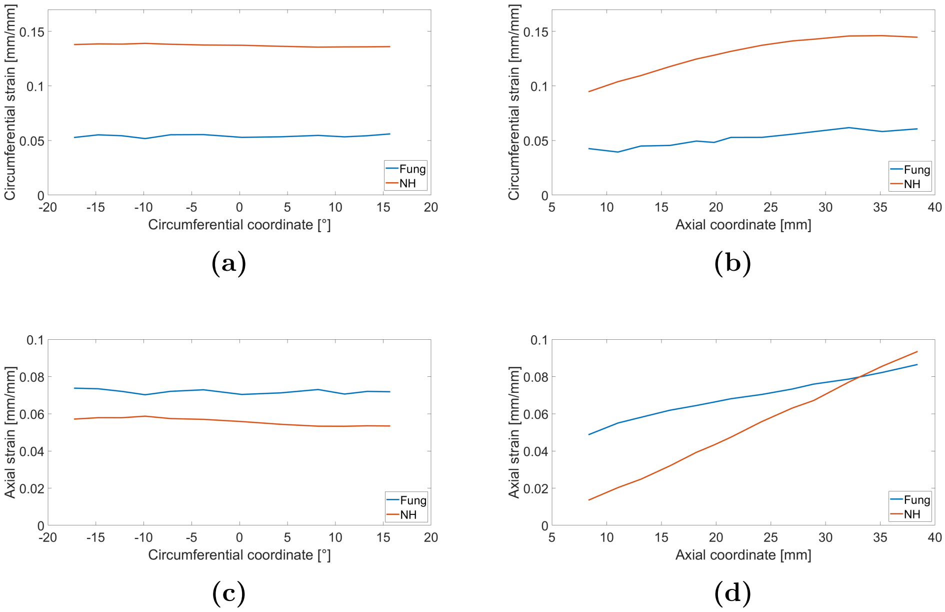

Figure 4.21: Circumferential strain of the ellipsoidal model in (a) circumferential direction, (b) axial direction, comparing Fung and Neo-Hookean models. Axial strain in (c) circumferential direction and (d) axial direction, comparing Fung and Neo-Hookean models.

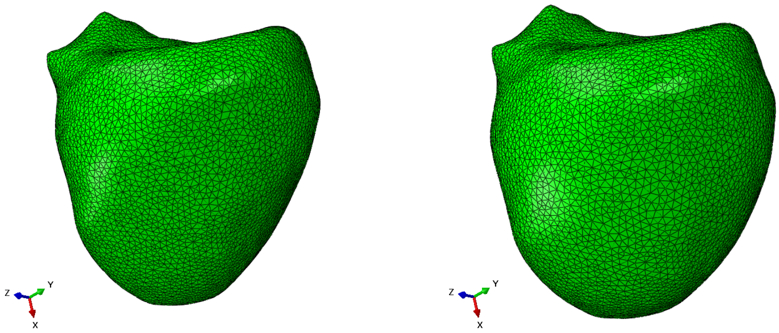

(a) t = 0 s **(b)** t = 1 s

Figure 4.22: Pressurization test on Neo-Hookean ventricle model at initial and final instants, with internal pressures equal to (a) 0 mmHg, and (b) 40 mmHg.

To evaluate the deformations experienced by cardiac tissue, creating a cylindrical reference system was unfeasible due to the absence of well-defined global axial and circumferential orientations in the model. As an alternative, a local Cartesian reference system was adopted in the heart region near the patch, as depicted in Figure 4.23. This approximation involved a local alignment of the x-direction with the circumferential one, the y-direction with the axial one and the z-direction with the radial one.

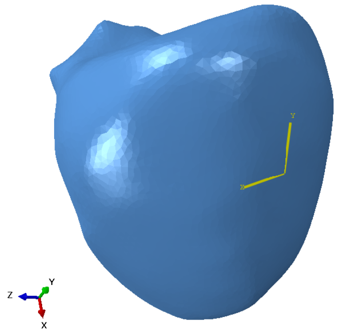

Figure 4.23: Local reference system in ventricle model.

Two paths were created as shown in Figure 4.24. For both, the approximated circumferential and axial deformations were extracted from the test, as shown in Figure 4.25.

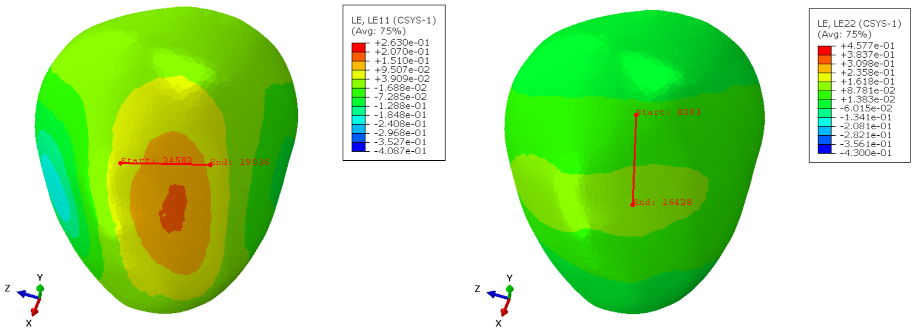
LE, LE11 (CSYS-1)
(Avg: 75%)
+2.630e-01
+2.070e-01
+1.510e-01
+9.507e-02
+3.909e-02
-1.688e-02
-7.285e-02
-1.288e-01
-1.848e-01
-2.408e-01
-2.968e-01
-3.527e-01
-4.087e-01
Start: 24582
End: 19036
Z
Y
X
LE, LE22 (CSYS-1)
(Avg: 75%)
+4.577e-01
+3.837e-01
+3.098e-01
+2.358e-01
+1.618e-01
+8.781e-02
+1.383e-02
-6.015e-02
-1.341e-01
-2.081e-01
-2.821e-01
-3.561e-01
-4.300e-01
Start: 8003
End: 16428
Z
Y
X

(a) **(b)**

Figure 4.24: Selection of two paths to evaluate deformations in the ventricle model. (a) Approximated circumferential strain field, (b) approximated axial strain field.

The healthy ventricle exhibited deformations in both directions of approximately 10%, aligning with existing literature findings [7, 9, 14]. In presence of the infarcted region, these strains decreased to a value around 2% due to the increased stiffness. However, the values returned comparable to those observed in healthy tissue outside the damaged area. When comparing the results with the ellipsoidal model, even though they employed different materials for healthy heart tissue, the conclusions drawn from the illustrated graphs remained consistent: the patch followed the deformation pattern of the infarcted heart, without having a negative impact on it.

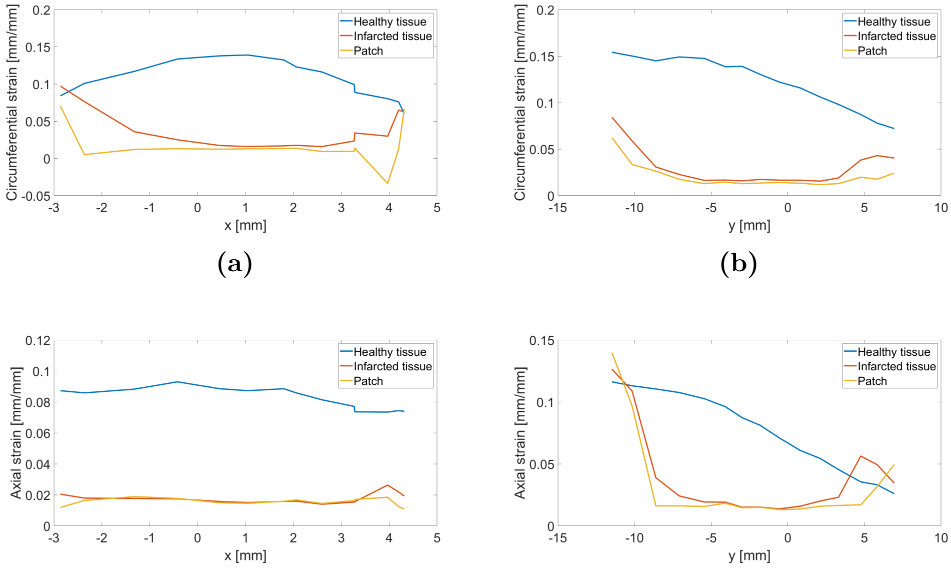

(a) **(b)**

(c) **(d)**

Figure 4.25: Approximation of circumferential strain of the ventricle model in (a) x-direction, (b) y-direction. Approximation of axial strain in (c) x-direction and (d) y-direction.

Chapter 5

Simulation of the electrophysiology of the heart

To verify that the designed patch was able to transmit the action potential conducted through myocardial cells, an *in silico* model was created. The Ten Tusscher's model was used. It is a mathematical model of the electrophysiological behaviour of human ventricular cells, based on the most important ionic currents involved in the generation of the action potential. The membrane is modeled as a capacitor connected in parallel with various resistances and bacteries representing ionic currents and pumps, respectively. The electrophysiological behavior of cells is described through a differential equation (Equation 5.1) as function of the current applied through a stimulus and the sum of all transmembrane ionic currents.

$$C_m \frac{dV}{dt} = -I_{stim} - I_{ion} \tag{5.1}$$

where C_m is cell capacitance per unit surface area, V is voltage, t is time, I_{stim} is the externally applied stimulus current, and I_{ion} is the sum of all transmembrane ionic currents, defined as

$$I_{ion} = I_{Na}+I_K+I_{to}+I_{Kr}+I_{Ks}+I_{CaL}+I_{NaCa}+I_{NaK}+I_{pCa}+I_{pK}+I_{bCa}+I_{bNa} \tag{5.2}$$

where I_{Na} is the fast Na^+ current, I_K is the inward rectifier K^+ current, I_{to} is the transient outward current, I_{Kr} is the rapid delayed rectifier current, I_{Ks} is the slow delayed rectifier current, I_{CaL} is the L-type Ca^{2+} current, I_{NaCa} is the Na^+/Ca^{2+} exchanger current, I_{NaK} is the Na^+/K^+ pump current, I_{pCa} and I_{pK} are *plateau* Ca^{2+} and K^+ currents, and I_{bCa} and I_{bNa} are the background Ca^{2+} and Na^+ leakage currents.

These currents in turn are described by equations whose coefficients are derived experimentally [63, 64].

5.1 Creation of the input files

To simulate the cardiac action potential propagation, *LS-Dyna* (Ansys Inc., 2022), an advanced multiphysics simulation software, was used.

For simplicity and greater practicality, four input files were created in order to separate the commands according to the field in which they were involved. They were written in *.k* format, that stands for key-file (i.e., built up of keywords [28]), and were called *main.k*, *struc.k*, *mesh.k* and *em.k*.

The *main.k* file contains parameters that are used in other files, making it more convenient to modify them afterwards. Among these parameters, there are the value of the time increment between one calculation step and the following one, and the time increment between one state of graphical display of the results and the following one. For the purpose of this thesis, the most relevant parameters were the ones regarding electrophysiology, that are the conductivity values of both the cardiac tissue and the patch, the surface-to-volume ratio and the cell capacitance per unit surface area.

The *struc.k* file declares how many parts the model is divided into, so that it is possible to assign to each part the proper material, defined in this same file. It also contains a parameter that establishes the duration of the propagation phenomenon to be simulated.

The *mesh.k* file contains the list of elements into which the model is divided. For each element, the part to which it belongs and the nodes that make it up are specified. There is also the list of nodes with their spatial coordinates. For the simulations that will be described in the following paragraphs, it was necessary to define some sets of nodes from which a stimulus started. These sets are defined in this file.

The *em.k* file contains all keywords regarding electrophysiology. One of them establishes the solving method of the problem, which, in the case of interest, can be electrophysiology bidomain or electrophysiology monodomain. The former represents the most complete model of cardiac electrical activity and it consists of two equations describing intra and extracellular potentials, coupled with a system of equations describing ionic currents, as it follows.

$$\begin{cases} \chi C_m \frac{\partial v}{\partial t} - div(D_i \nabla u_i) + \chi I_{ion}(v,w) = I^i_{app} \\ \\ -\chi C_m \frac{\partial v}{\partial t} - div(D_e \nabla u_e) - \chi I_{ion}(v,w) = -I^e_{app} \\ \\ \frac{\partial w}{\partial t} - R(v,w) = 0, \quad v(\mathbf{x},t) = u_i(\mathbf{x},t) - u_e(\mathbf{x},t) \end{cases} . \tag{5.3}$$

where u_i and u_e are the intra and extracellular potentials, v is the transmembrane potential, w represents the gating and concentration variables, and the coefficient χ is the ratio of membrane area per tissue volume. $I_{ion}(v,w)$ is the ionic current described before, and R is a function that, together with I_{ion}, depends on the membrane model employed. D_i and D_e are the conductivity tensors of the intra and the extracellular medium, $\mathbf{x}$ is the position in the myocardium, and $I^{i,e}_{app}$ are the applied currents per unit volume.

The electrophysiology monodomain is a simplified model and consists of an equation describing the evolution of the transmembrane potential coupled with an ionic model (Equation 5.4). For this reason, it is less computationally expensive and less time consuming [12].

$$\begin{cases} \chi C_m \frac{\partial v}{\partial t} - div(D(\mathbf{x}) \nabla v) + \chi I_{ion}(v,w) = I_{app} \\ \\ \frac{\partial w}{\partial t} - R(v,w) = 0 \end{cases} . \tag{5.4}$$

Each material defined in the *struc.k* file is associated with a keyword in the *em.k* file, that describes the behavior of the material from the electrical point of view, specifying the conductivity values. For the simulations that will be described, the conductive materials were active, meaning they can carry a source, or passive, meaning they are not connected to any current or voltage source. Every active material must be related to a cell model, such as Ten Tusscher's, which is already implemented in *LS-Dyna* and was defined in this file by expliciting the coefficients of the equations cited at the beginning of chapter 5.

The parameters of the applied stimuli were explicited here, in the *em.k* file. They are the set of nodes to which the stimulus was applied, the starting instant, the duration and the amplitude.

5.2 Simulations on simplified model

5.2.1 Input parameters

Since the primary aim of this thesis was to verify whether the patch was able to conduct the electrical stimulus by following the action potential of the heart, it was firstly used a simplified model of both the heart and the patch to better understand how to set up more realistic simulations afterwards.

Using *LS-PrePost* (Ansys Inc., 2022), the heart was represented with a parallelepiped measuring 60 x 24 x 6 mm following a model used in literature [47]. The patch was also represented with a parallelepiped, measuring 12 x 12 x 1 mm, positioned at the centre of the upper surface of the heart model and adherent to it, as shown in Figure 5.1.

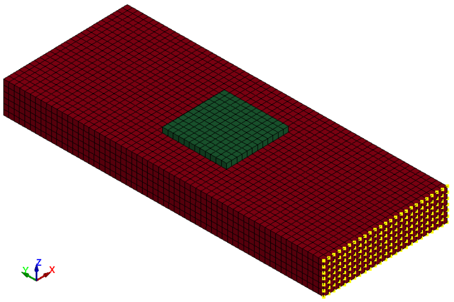

Figure 5.1: Simplified model of heart tissue and patch. The nodes highlighted in yellow constitute the set from which the stimulus starts.

To simulate an infarct, a region with a square cross-section of 8 x 8 mm was created below the patch and through the entire thickness of the heart tissue model, as shown in Figure 5.2.

The assembly obtained was thus composed of three distinct parts, for which a mesh was created with *brick* elements of dimension 1 x 1 x 1 mm. Note that, for the correct functioning of the software, the nodes in the regions where the parts are in contact must be coincident.

The electrophysiological parameters set are 140 μm^{-1} for the surface area to volume ratio and 0.01 $\mu F/mm^2$ for the cell capacitance per unit surface area.

The conductivity values in direction x (S_{xx}), y (S_{yy}) and z (S_{zz}) for the three different parts are displayed in Table 5.1. The fibers were assumed to be oriented along y-direction.

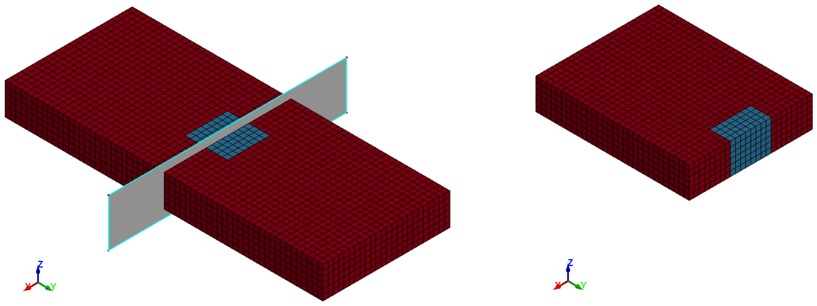

(a) (b)

Figure 5.2: Simplified model of heart tissue and infarcted region. (a) Complete model with section plane in evidence. (b) Section of the model.

Table 5.1: Conductivity values in direction x, y and z for heart, infarct and rectangular patch.

	S_{xx} [S/m]	S_{yy} [S/m]	S_{zz} [S/m]
Heart tissue	0.06	0.2	0.06
Infarcted tissue	0	0	0
Patch	3.9	3.9	3.9

The values for healthy heart tissue correspond to the conductivity values found in literature [8, 14, 22]. For the infarct, zero conductivity was set since this type of scar tissue does not contain cardiomyocytes and therefore does not conduct the action potential. The conductivity of the material selected in section 2.3 was used for the patch [19].

The stimulus started from the nodes of the face shown in Figure 5.1 of the parallelepiped model of the heart, following the path in a longitudinal direction and crossing both the infarct and the patch.
This stimulus had the characteristics shown in Table 5.2, corresponding to a healthy heartbeat with a frequency of 60 bpm (i.e., beats per minute).

Table 5.2: Parameters of the stimulus.

Starting instant [ms]	Duration [ms]	Amplitude [mV]	Period [ms]
0	2	50	1000

5.2.2 Results and discussion

To assess the patch performance under the most basic conditions, simulations were initially conducted on healthy tissue alone. This allowed to validate the electrophysiological parameters of the model. Subsequently, it was introduced the infarcted area, and finally, the patch was incorporated into the simulations. Given the simplicity of the model, bidomain was chosen due to its greater precision.

The transmembrane potential was evaluated for healthy heart tissue and infarcted region, constituted by active conductive materials. In contrast, the patch, a passive conductive material, lacks a transmembrane potential, so only its external potential was considered.

The outcomes, shown in Figure 5.3 and Figure 5.4, indicated that the patch efficiently conducted the external potential transmitted by the heart, enabling the transition to a more realistic model.

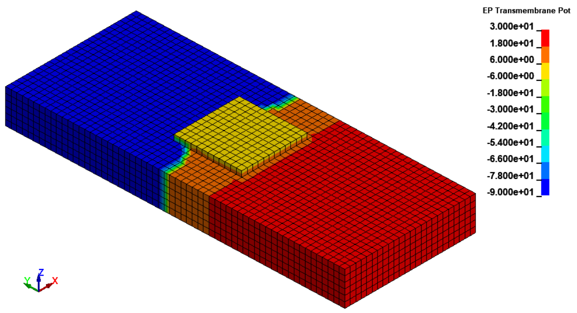
EP Transmembrane Pot
3.000e+01
1.800e+01
6.000e+00
-6.000e+00
-1.800e+01
-3.000e+01
-4.200e+01
-5.400e+01
-6.600e+01
-7.800e+01
-9.000e+01
Z
Y
X

Figure 5.3: Transmembrane potential in a simplified model of the heart at instant t = 100 ms. The colorbar values are expressed in mV.

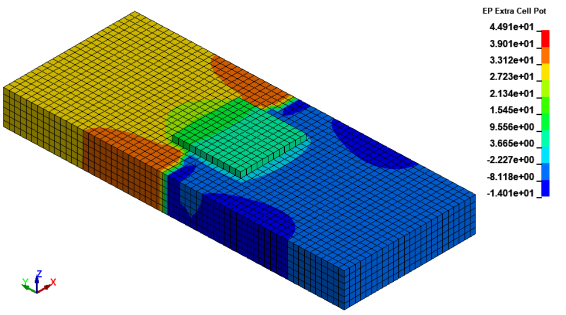
EP Extra Cell Pot
4.491e+01
3.901e+01
3.312e+01
2.723e+01
2.134e+01
1.545e+01
9.556e+00
3.665e+00
-2.227e+00
-8.118e+00
-1.401e+01
Z
Y
X

Figure 5.4: Extracellular potential in a simplified model of the heart at instant t = 100 ms.

Five distinct nodes, situated on the outer surface of the model (Figure 5.5), were selected: one belongs to the set of nodes from which the stimulus starts (i.e., node A), two are on the healthy tissue before and after the patch (i.e., nodes B and C), one on the infarct (i.e., node E, not visible in the figure), and the last on the patch (i.e., node D). The transmembrane and extracellular potentials corresponding to these designated points is graphically represented in Figure 5.6.

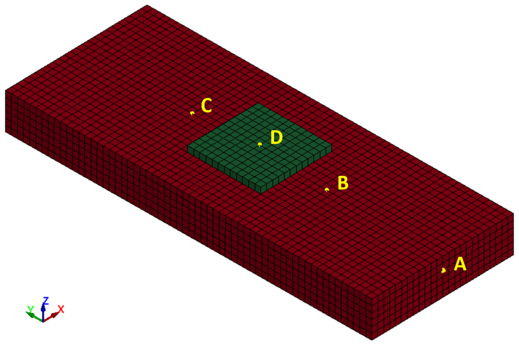

Figure 5.5: Selection of five nodes in the simplified model of the heart (the one on the infarcted region is not visible).

In healthy cardiac tissue, the resting transmembrane potential maintained a value of -85.23 mV, given by the difference between the negative intracellular potential and the positive extracellular potential. Once the stimulus began, the intracellular potential increased to positive values, while the extracellular potential decreased towards negativity. As a result, their disparity generated the positive peak in the action potential waveform (Figure 5.6a).

For the patch, the external potential had the same trend of the one of the healthy heart tissue, meaning the electric signal was correctly transmitted.

The infarct showed a constant transmembrane potential because it is a non-excitable region.

Table 5.3 presents the transmembrane potential characteristics of the node before and the node after the infarcted region (i.e., nodes B and C), derived using a *Matlab* code. These attributes are the action potential amplitude (APA [mV]), the action potential duration at 90% of the repolarization (APD_{90} [ms]), the value of maximum upstroke (dV/dt max [mV/ms]), the resting membrane potential (RMP [mV]), and the maximum value of potential itself (V_{max} [mV]).

Analyzing the action potential characteristics of nodes B and C, they remained unaffected by the presence of the patch.

The only difference between node B and node C was in the activation time, that had a value of 58.8 ms and 135.54 ms, respectively, as they were sequentially activated.

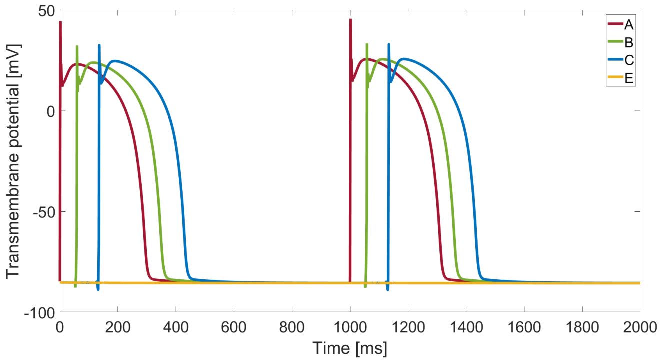

(a)

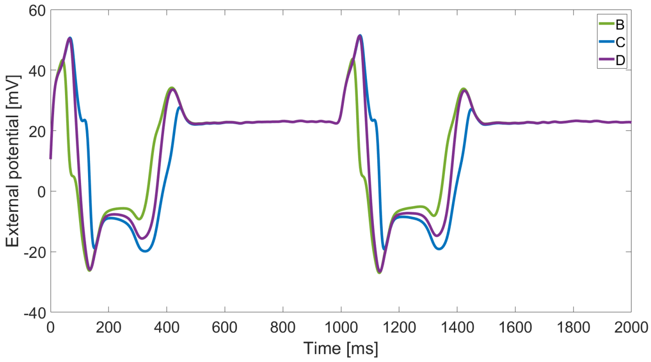

(b)

Figure 5.6: (a) Transmembrane and (c) external potentials of selected nodes.

Table 5.3: Action potential characteristics for nodes B and C in the simplified model, the first before and the second after the infarcted region.

	APA	APD	dV/dt max	RMP	V_{max}
Node B	120.19	294.81	330.41	-85.23	32.39
Node C	121.44	298.91	345.25	-85.23	32.53

5.3 Simulations on heart model

5.3.1 Input parameters

To verify that the patch was capable of conducting the action potential in a more realistic configuration, the heart model described in chapter 3 was used. An infarcted region was added to this model and, above it, a parallelepiped-shaped patch that adapts to the curvature of the heart had been added, following the same procedure described in subsection 4.3.1. The decision to use a simplified patch was made to avoid overly complicating the model.

The model with and without the patch is shown in Figure 5.7.

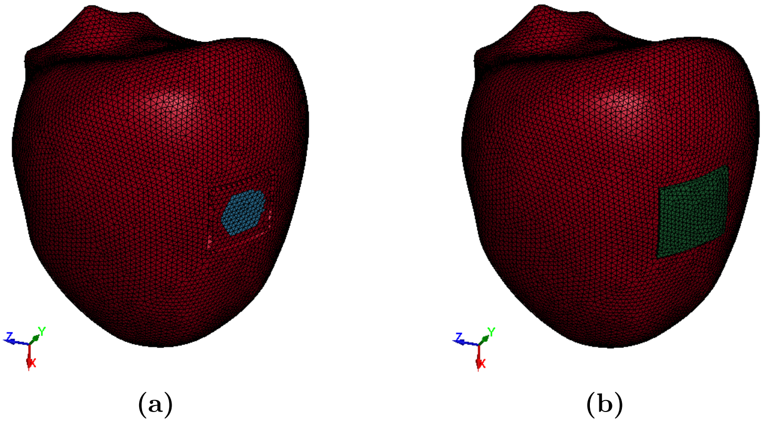

(a) (b)

Figure 5.7: Model of heart tissue with (a) an infarcted region, and (b) a patch above it.

The mesh was generated with tetrahedral elements with an average side length of 1.5 mm.

The electrophysiological parameters, i.e., electrical conductivities, surface area to volume ratio and cell capacitance per unit surface area, were kept the same as those described in subsection 5.2.1.

Remaining consistent with the physiological propagation of the action potential in the ventricle, the stimulus started from the apex and moved towards the base, and from the endocardium towards the epicardium. Consequently, a set of nodes was created in the inner wall of the model in the apical part, as shown in Figure 5.8.
This stimulus had the same characteristics that were reported in Table 5.2.

In order to test the conductivity of the patch also in an anomalous situation, an extra systole was simulated by creating a second set of nodes, shown in Figure 5.9, from which a stimulus with the characteristics exposed in Table 5.4 started.

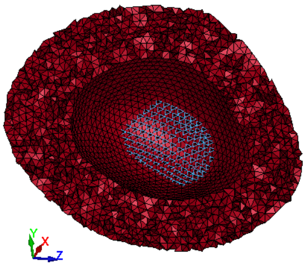

Figure 5.8: Set of nodes from which the stimulus started in the ventricle model seen in a transversal section.

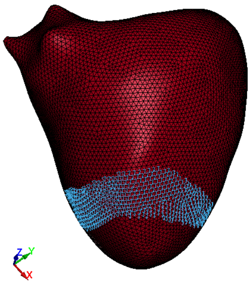

Figure 5.9: Set of nodes from which the extra stimulus started in the ventricle model. Unlike the first stimulus, this one was realised throughout the entire thickness of the myocardium.

This case corresponded to an arrhythmia with spiral waves that were created by the extra stimulus in the refractory tail of the wave generated by the first stimulus [27].

Table 5.4: Parameters of the extra stimulus [27].

Starting instant [ms]	Duration [ms]	Amplitude [mV]	Period [ms]
410	2	200	200000

5.3.2 Results and discussion

In order to determine the appropriate resolution method to employ, two simulations were performed using identical inputs. The only variable altered between the simulations was the parameter that differentiates monodomain from bidomain.

For the sake of simplicity, a physiological heart beat was simulated using the healthy ventricle model. The differences between these two simulations are visually depicted in Figure 5.10. Notably, the temporal evolution of action potential propagation exhibited distinct patterns. Indeed, when observing the same time instants, the active and refractory zones showed disparate characteristics and involved varying regions of the heart.

If the behavior had remained unaltered between monodomain and bidomain, the former would have been preferred due to its reduced computational requirements. In this case, however, the evolution of the action potential was visibly different, so the bidomain method was chosen, given its higher accuracy.

Physiological heartbeat

A physiological heartbeat was simulated under three distinct conditions: one with entirely healthy heart tissue, another with the presence of an infarct, and the last with a patch applied over the damaged region (Figure 5.11).

The transmembrane potential was assessed for active conductive materials (i.e., healthy heart tissue and infarcted region), as they possess both intracellular and extracellular potentials. In contrast, the patch, being a passive conductive material, lacks a transmembrane potential, and consequently, only its external potential was considered.

Figure 5.11 displays how the infarct, having zero conductivity, did not propagate the action potential. Conversely, the potential conducted by the patch aligned with the extracellular potential of the heart.

In Figure 5.12, it is displayed the selection of three distinct nodes situated on the outer surface of the ventricle: one within the infarcted region (i.e., node C), another in the healthy tissue immediately below the infarct (i.e., node A), and the third in the healthy tissue above the affected area (i.e., node B).

The transmembrane potential corresponding to each of these designated points is graphically represented in Figure 5.13, and shows how, in presence of an infarct, the trasmembrane potential of that region remained

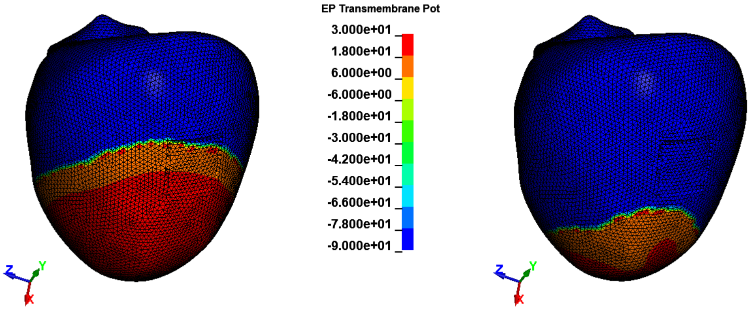
EP Transmembrane Pot
3.000e+01
1.800e+01
6.000e+00
-6.000e+00
-1.800e+01
-3.000e+01
-4.200e+01
-5.400e+01
-6.600e+01
-7.800e+01
-9.000e+01
Z
Y
X

(a) t = 100 ms **(b)** t = 100 ms

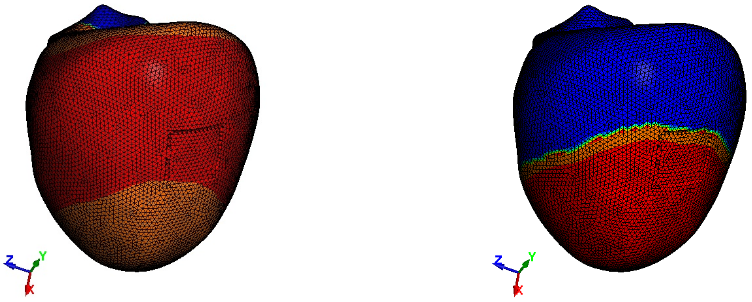

(c) t = 200 ms **(d)** t = 200 ms

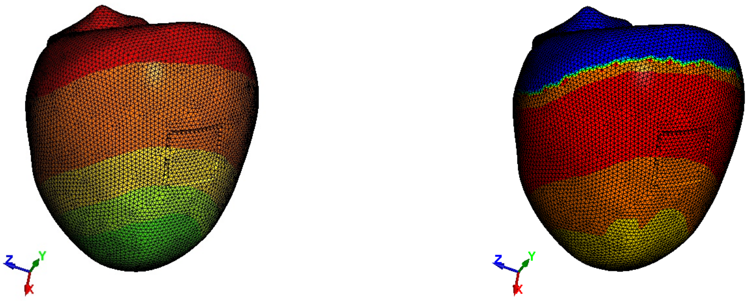

(e) t = 300 ms **(f)** t = 300 ms

Figure 5.10: Temporal evolution of the action potential using monodomain (a,c,e) and bidomain (b,d,f) at corresponding time instants. The colorbar values are expressed in mV.

at its resting value (Figure 5.13b).

A node on the patch (i.e., node D) was selected to show its conductivity properties, shown in Figure 5.14. Here, the transmembrane potential conducted by the patch was zero, since it is a passive material. Conversely, the patch was able to follow the extracellular potential of the heart tissue (Figure 5.14b).

Table 5.5 presents the action potential characteristics of nodes A and B (i.e., before and after the infarcted region), derived using a *Matlab*

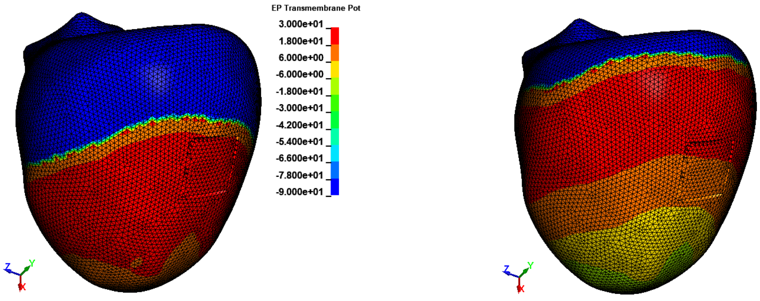
EP Transmembrane Pot
3.000e+01
1.800e+01
6.000e+00
-6.000e+00
-1.800e+01
-3.000e+01
-4.200e+01
-5.400e+01
-6.600e+01
-7.800e+01
-9.000e+01
Z
Y
X

(a) t = 220 ms **(b)** t = 320 ms

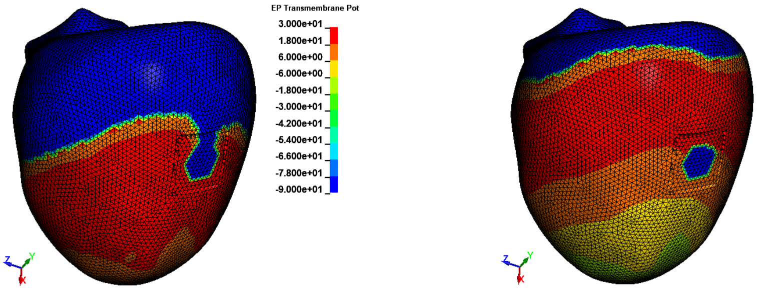
EP Transmembrane Pot
3.000e+01
1.800e+01
6.000e+00
-6.000e+00
-1.800e+01
-3.000e+01
-4.200e+01
-5.400e+01
-6.600e+01
-7.800e+01
-9.000e+01
Z
Y
X

(c) t = 220 ms **(d)** t = 320 ms

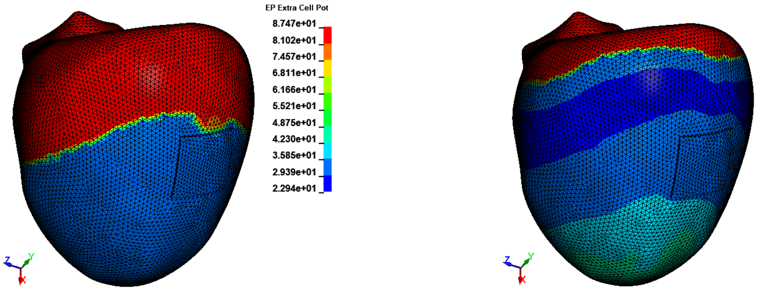
EP Extra Cell Pot
8.747e+01
8.102e+01
7.457e+01
6.811e+01
6.166e+01
5.521e+01
4.875e+01
4.230e+01
3.585e+01
2.939e+01
2.294e+01
Z
Y
X

(e) t = 220 ms **(f)** t = 320 ms

Figure 5.11: Propagation of transmembrane potential in (a,b) healthy heart and (c,d) tissue with infarct. (e,f) Propagation of extracellular potential in presence of a patch.

code. These attributes are the same exposed in subsection 5.2.2 and are referred to three distinct simulations: one with healthy tissue (HT), one with infarcted tissue (IT) and one with infarcted tissue and patch (P).

Action potential characteristics of nodes A and B remained unaltered in the presence of both the infarct and the patch. For node B, when damaged tissue was present, the activation time increased to 231.16 ms compared to the case of healthy tissue (i.e., 205.17 ms). Introducing the patch mitigated this delay, reducing it by a few milliseconds, being the activation time in this case equal to 225.77 ms.

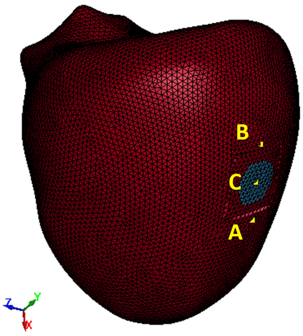

Figure 5.12: Selection of three nodes on heart tissue.

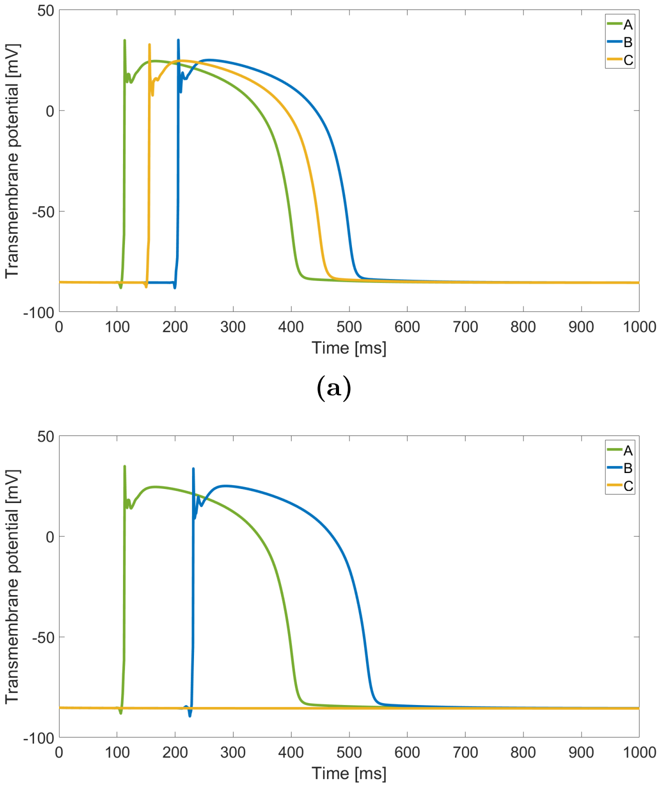

(a)

(b)

Figure 5.13: Temporal evolution of action potential in three nodes of the heart. (a) Healthy heart tissue, (b) heart tissue with an infarcted region.

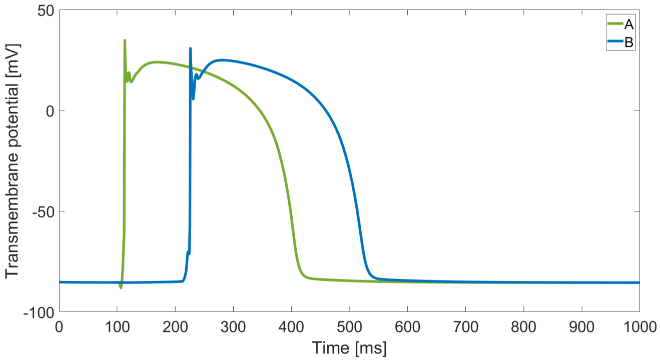

(a)

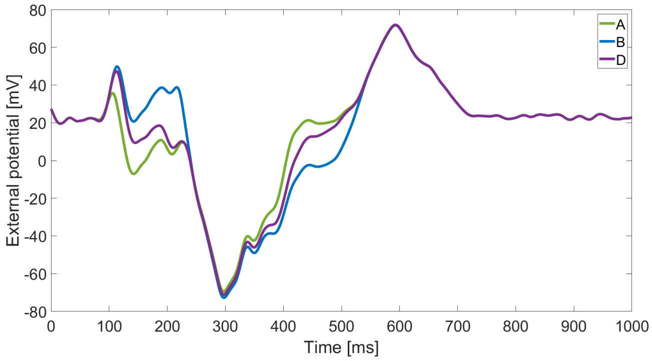

(b)

Figure 5.14: Temporal evolution of potentials in two nodes of the heart (A and B) and one on the patch (D). (a) Transmembrane, (b) extracellular potentials.

Table 5.5: Action potential characteristics for nodes A and B, the first before and the second after the infarcted region.

		APA	APD	dV/dt max	RMP	V_{max}
Node A	HT	122.93	294.87	340.69	-85.23	34.78
	IT	122.93	294.87	340.70	-85.23	34.78
	P	122.97	296.67	340.81	-85.23	34.83
Node B	HT	123.21	300.19	341.14	-85.23	34.98
	IT	123.14	305.13	345.47	-85.23	33.61
	P	116.34	300.23	303.94	-85.23	30.82

Extrasystole

In accordance with what was delineated in subsection 5.3.1, the examination of healthy heart tissue, a ventricle afflicted by infarction, and a ventricle with both infarct and patch was conducted, running simulations to emulate the occurrence of an extrasystole and test the conductivity of the patch also in this anomalous situation. The attributes of the extra stimulus are the ones previously exposed in Table 5.4.

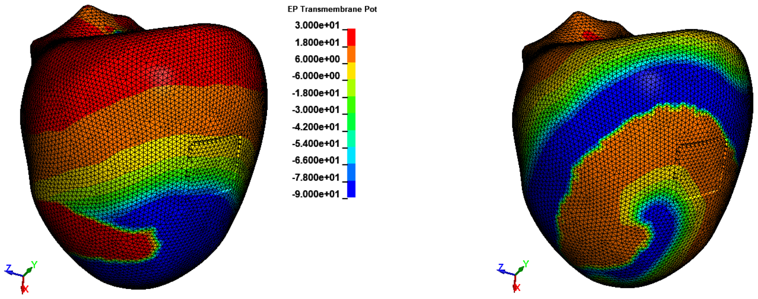
EP Transmembrane Pot
3.000e+01
1.800e+01
6.000e+00
-6.000e+00
-1.800e+01
-3.000e+01
-4.200e+01
-5.400e+01
-6.600e+01
-7.800e+01
-9.000e+01
Z
Y
X

(a) t = 420 ms **(b)** t = 1000 ms

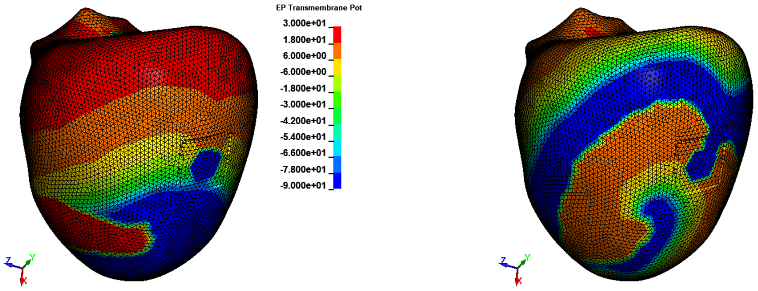
EP Transmembrane Pot
3.000e+01
1.800e+01
6.000e+00
-6.000e+00
-1.800e+01
-3.000e+01
-4.200e+01
-5.400e+01
-6.600e+01
-7.800e+01
-9.000e+01
Z
Y
X

(c) t = 420 ms **(d)** t = 1000 ms

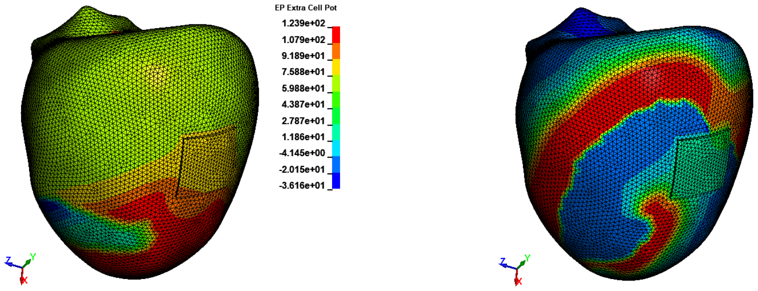
EP Extra Cell Pot
1.239e+02
1.079e+02
9.189e+01
7.588e+01
5.988e+01
4.387e+01
2.787e+01
1.186e+01
-4.145e+00
-2.015e+01
-3.616e+01
Z
Y
X

(e) t = 420 ms **(f)** t = 1000 ms

Figure 5.15: Propagation of transmembrane potential with extrasytole in (a,b) healthy heart and (c,d) tissue with infarct. (e,f) Propagation of extracellular potential in the same situation in presence of a patch.

For the active materials, i.e., the healthy tissue and the infarct, the transmembrane potential was examined, while the external potential was used to determine the behaviour of the patch when subjected to an action potential.

Figure 5.15 illustrates how the additional stimulus initiated a spiral-shaped action potential, mimicking a possible cardiac arrhythmia. This happened because the action potential originating from the second set of nodes encountered cardiac tissue that had not yet returned to its resting potential. Instead, it interacted with regions that were still in a refractory state and therefore could not be stimulated. The potential propagated exclusively through excitable heart tissue and extended to other zones only once they had exited the refractory state. It is evident that the infarcted region remained incapable of conducting the action potential carried by the healthy tissue. Conversely, the patch effectively transmitted the extracellular potential.

The transmembrane potential of the same three nodes displayed in Figure 5.12 is graphically represented in Figure 5.16 and shows how, in presence of an infarct, the trasmembrane potential of that region remained at its resting value (Figure 5.16b).

As explained in the previous paragraph, a node on the patch (i.e., node D) was selected to show its conductivity properties, as shown in Figure 5.17. Here, the transmembrane potential conducted by the patch was zero since it is a passive material (Figure 5.17a). Conversely, the patch was able to follow the extracellualar potential of the heart tissue (Figure 5.17b).

Table 5.6 presents the action potential characteristics of the nodes A and B (i.e., before and after the infarcted region), derived using a *Matlab* code. These attributes are the same exposed in the previous paragraph, with the distinction that the action potential under consideration here (Figure 5.17a) was not the initial one, which represents the physiological beat, but the second, which represents the additional stimulus. The results are referred to three distinct simulations: one with healthy tissue (HT), one with infarcted tissue (IT) and one with infarcted tissue and patch (P). Action potential characteristics remained unaffected by the presence of the patch.

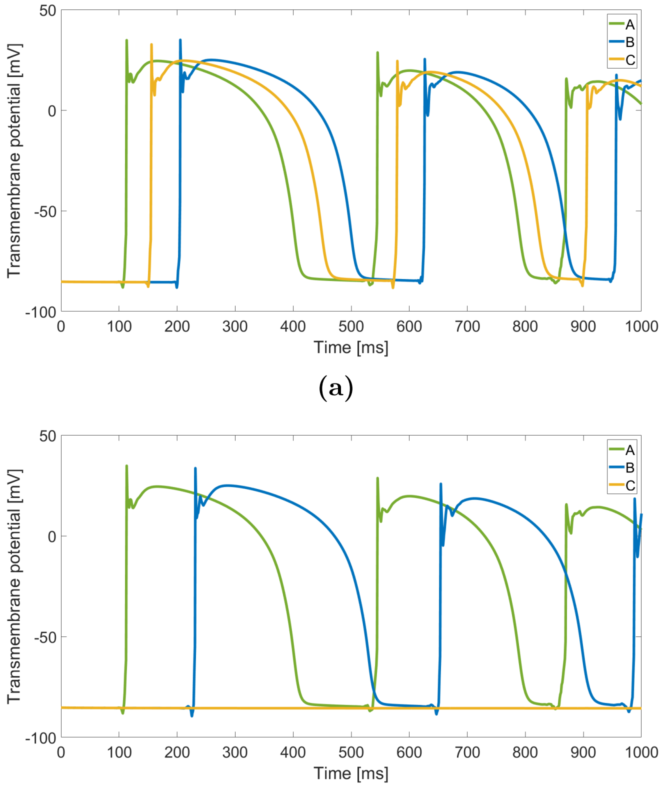

(a)

(b)

Figure 5.16: Temporal evolution of action potential in three nodes of the heart in presence of an extrasystole. (a) Healthy heart tissue, (b) heart tissue with an infarcted region.

Table 5.6: Action potential characteristics for nodes A and B, the first before and the second after the infarcted region, in presence of extrasystole.

		APA	APD	dV/dt max	RMP	V_{max}
Node A	HT	115.65	251.32	263.78	-85.23	28.69
	IT	115.65	251.38	263.77	-85.23	28.68
	P	115.39	250.58	263.11	-85.23	29.48
Node B	HT	111.46	249.41	252.45	-85.23	25.42
	IT	114.41	253.35	257.95	-85.23	25.84
	P	113.54	252.55	259.00	-85.23	25.37

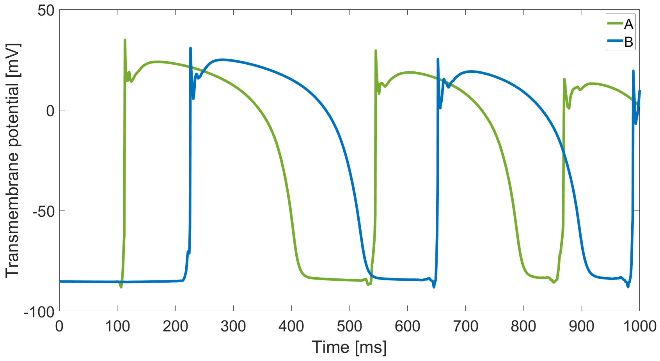

(a)

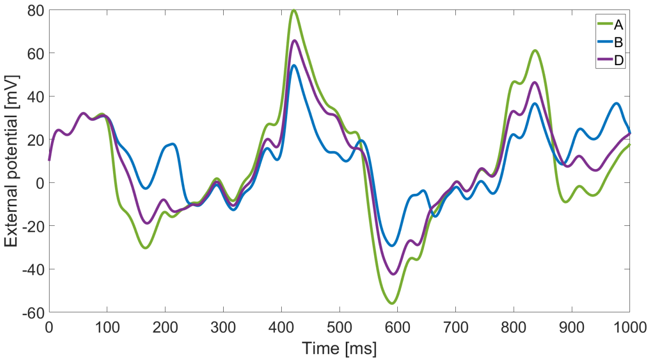

(b)

Figure 5.17: Temporal evolution of potentials in two nodes of the heart (A and B) and one on the patch (D), with an extrasystole. (a) Transmembrane, (b) extracellular potentials.

5.4 Simulations with auxetic patch

5.4.1 Input parameters

After achieving promising conductivity outcomes, the model underwent further refinement by substituting the simplified patch with the auxetic geometry selected in section 2.3. The solid patch was generated with the same procudere described in subsection 4.1.1, and it was meshed with tetrahedral elements of average size equal to 0.15 mm.

The healthy heart tissue was still represented by a parallelepiped that was meshed using tetrahedral elements.

Since the nodes of the patch must coincide with those of the parallelepiped, the mesh generated on the latter is not uniform. Specifically, the average dimension of elements at parallelepiped extremities measures approximately 1.5 mm, but this value decreases moving towards the central area where the patch is situated.

The infarct was generated as a set of elements in *Abaqus* and converted into a part, enabling the assignment of distinct conductive properties to it. The model is shown in Figure 5.18.

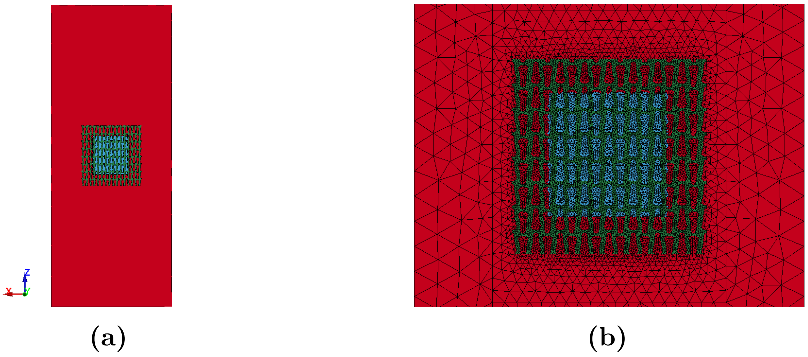

(a) **(b)**

Figure 5.18: Parallelepiped-shaped model of heart tissue (60 x 24 x 6 mm), infarct and auxetic patch (12 x 12 x 0.6 mm). (a) Complete model (b) Enlargement of patch.

The electrophysiological parameters (i.e., electrical conductivities, surface area to volume ratio and cell capacitance per unit surface area) are the same as the ones described in subsection 5.2.1.

The conductivity values in direction x (S_{xx}), y (S_{yy}) and z (S_{zz}) for the three different parts were kept the same as those displayed in Table 5.1. The different conductive properties of the patch in the two directions were ensured by the auxetic geometry.

The set of nodes from which the stimulus started and its parameters are the same as those illustrated in Figure 5.1 and in Table 5.2.

5.4.2 Results and discussion

To evaluate the conductivity of the patch with its actual geometry, results were estracted similarly to those delineated in section 5.2 and section 5.3.

Figure 5.19 and Figure 5.20 provide representations of the transmembrane potential and extracellular potential at a specific time instant. These visuals suggest that the patch effectively conducted the stimulus similarly to the behavior observed in cardiac tissue.

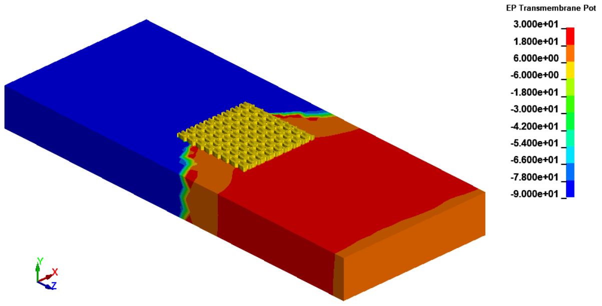
EP Transmembrane Pot
3.000e+01
1.800e+01
6.000e+00
-6.000e+00
-1.800e+01
-3.000e+01
-4.200e+01
-5.400e+01
-6.600e+01
-7.800e+01
-9.000e+01
Y
X
Z

Figure 5.19: Transmembrane potential in a simplified model of the heart with an auxetic patch at instant t = 140 ms.

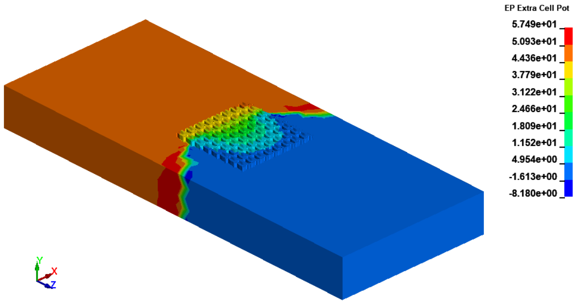
EP Extra Cell Pot
5.749e+01
5.093e+01
4.436e+01
3.779e+01
3.122e+01
2.466e+01
1.809e+01
1.152e+01
4.954e+00
-1.613e+00
-8.180e+00
Y
X
Z

Figure 5.20: Extracellular potential in a simplified model of the heart with an auxetic patch at instant t = 140 ms.

To gain a more comprehensive insight into the patch performance over the entire duration of a heartbeat (i.e., 1000 ms), three nodes were examined: one on the patch and two on the surrounding healthy heart tissue, one before and one after the patch region.

The diagrams in Figure 5.21 display the temporal evolution of stimulus propagation and the external potential.

Five nodes were chosen using a method similar to the one depicted in Figure 5.5. Analyzing the action potential characteristics of nodes before (i.e., node B) and after the patch (i.e., node C), they remained unaffected by the presence of the patch, as it is illustrated in Table 5.7. As observed in the previously examined cases, the parameter that underwent a noticeable variation from node B to node C was the activation time, that was equal to 96.82 milliseconds and 170.9 milliseconds, respectively, since the action potential required a specific time interval to propagate.

In the context of this thesis, the electrical problem was addressed alongside the mechanical one. As a result, incorporating the auxetic geometry patch into the electrical simulations ensured that its usage didn't interfere with conduction. Once the conductivity of both solutions is confirmed, the choice between an auxetic and non-auxetic patch hinges primarily on the results of the mechanical tests.

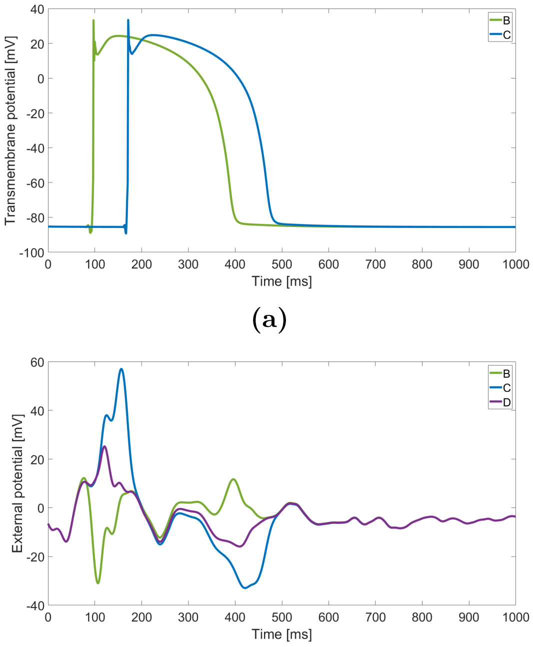

(a)

(b)

Figure 5.21: Temporal evolution of potentials in the nodes before (B) and after (C) the patch and on the patch itself (D). (a) Transmembrane potential, (b) extracellular potential.

Table 5.7: Action potential characteristics for nodes B and C, the first before and the second after the auxetic patch.

	APA	APD	dV/dt max	RMP	V_{max}
Node B	122.21	296.86	346.33	-85.23	33.36
Node C	122.81	302.30	334.85	-85.23	33.52

Chapter 6

Conclusions

Myocardial ischemia occurs when myocardial cells experience suffering or damage due to an inadequate oxygen supply in relation to their metabolic requirements. The site of a myocardial infarction depends on the occluded coronary artery, but usually necrosis affects the left ventricular and septal myocardium, mainly in the subendocardial layer or in the entire thickness of the damaged region.

If myocardial cell death occurs due to prolonged oxygen deficiency (i.e., ischemia), the loss of contractile function in the affected area will become persistent. The larger the infarcted region, the more significant the reduction in the contractile function of the left ventricle and, consequently, the overall function of the heart. Myocardial ischemia not only affects ventricular contraction but also disrupts ventricular relaxation, impeding the normal filling of the ventricle. Furthermore, it significantly alters also the electrical properties of myocardial cells, many of which are maintained by oxygen-consuming ion pumps, leading to irregularities in the depolarization and/or repolarization phases.

Currently, there are no established clinical approaches for treating an acute myocardial infarction. However, preventive procedures are employed to mitigate the condition in patients afflicted with chronic ischemic heart disease. The treatment goals for these individuals are dual, involving the reduction of the risk of severe coronary events such as death or infarction, as well as the alleviation of ischemia severity.

The literature analysis performed at the beginning of this work indicates that currently no devices or technologies that can be used to repair and treat the infarcted area of the myocardium exist, except for a few solutions that only aim to regenerate damaged cardiac or vascular tissue, like pericardial closure, valve and annulus repair and great vessel reconstruction [24, 29]. The application of technologies based on stem cells to treat acute myocardial infarction is also being explored by other companies, but these studies are still in the clinical trial stage [26].

The devices approved for clinical application are not curative solutions. Indeed, they offer only tissue regeneration capabilities and lack the ability to establish electrical integration with the tissue [8].

A promising emerging field of research focuses on myocardial tissue engineering, employing hydrogels, scaffolds, and patches to facilitate the support and replacement of damaged tissue through both cellular and non-cellular methods.

Considering acellular patches, it is crucial not only to substitute the electrical properties lost by the infarcted tissue, but also to ensure that the applied patch does not impair the normal function of the heart. Therefore, the mechanical properties of the patch should closely resemble those of the heart tissue, with minimal alteration to the established deformation state during the cardiac cycle.

The first part of this thesis aimed at assessing the feasibility of using an optimization tool to achieve a patch geometry having the desired mechanical properties. The employed code was well-suited for this purpose. In fact, this approach requires only a limited knowledge of the bulk material properties and it allows to avoid the long and iterative adjustments of parameters, typically required when working with existing geometries.

Moreover, the outcome of the tool demands minimal post-processing to be utilized for the creation of a CAD model for subsequent analysis.

For these reasons, this methodology can extend beyond its current application and be leveraged for crafting medical devices designed to mend various biological structures, such as arteries, lung tissue, skin, liver, and more. The inherent flexibility of the code allows for effortless modification of the objective function and matrix elements under control, facilitating adaptability to diverse applications.

The mechanical simulations conducted in the second part of the thesis involved assessing the impact of a patch on the deformation state of the ventricle during the cardiac cycle, using both simplified and non-simplified models.

It can be concluded from the results of this work that the application of a patch onto a damaged area of the heart did not remarkably influence the strain field already altered by the presence of the infarct. As expected, incorporating this device without removing the necrotic region cannot restore the deformations that characterize the completely healthy tissue, because the scar tissue has a high and not-modifiable stiffness.

The device was made auxetic through the creation of a pattern, based on the assumption that cardiac tissue exhibits a negative Poisson's ratio. Consequently, benefits were expected from using an auxetic patch, since its properties closely resembled those of heart tissue. Nonetheless, simulations conducted on the simplified model revealed that the performance of the auxetic patch did not significantly diverge from that of a patch with a positive Poisson's coefficient.

This outcome is potentially caused by the various limitations inherent in the conducted tests. Therefore, a more precise inference regarding the expected benefits can be derived through the implementation of more rigorous simulations.

The electrophysiological problem, examined in the third part of the thesis, was aimed at assessing the conductivity of the patch in terms of its ability to conduct the action potential transmitted by the myocardial cells, both in the case of a physiological beat and in more abnormal situations such as the presence of an extra systole.

The results indicated that the patch was indeed capable of conducting the electrical stimulus in the illustrated cases, while maintaining the essential parameters defining the action potential. Consequently, this device stands as a versatile solution for situations in which a conductive substrate is necessary. An example is the cultivation and differentiation of myocardial cells that require stimulation for their growth.

Moreover, as a result of applying the patch, there was a slight reduction in signal propagation delay attributed to the presence of the infarct.

Within the scope of this thesis, the electrical problem was addressed concurrently with the mechanical one. Consequently, the inclusion of the patch with auxetic geometry in the electrical simulations allowed to ensure that its utilization did not disrupt conduction. After confirming the actual conductivity of both solutions, the selection between an auxetic and non-auxetic patch primarily depends on the outcomes of the mechanical tests.

The primary limitation of this study was the selection of materials for the healthy and infarcted heart tissue as well as the patch. In particular, the application of Fung's material to a four-layer model introduced a significant approximation, which deviates from the anatomical three-dimensional architecture of ventricular musculature that naturally comprises multiple layers. Moreover, the coefficients associated with this material were experimentally derived from porcine hearts and presented considerable variability across the limited number of samples analyzed. Additionally, while a precise local reference system indicating the orientation of the fibers was meticulously created for each layer of the parallelepiped-shaped model, the same level of precision was not achieved for the ellipsoidal one. For the latter, the reference systems were roughly assigned to small circular sectors and did not adequately account for the curvature at the apex of the model. For a more rigorous approach, it is advisable to establish a local reference system for each mesh element, ensuring greater accuracy and reliability in the analysis.

To overcome these limitations, cardiac tissue should be modelled using materials that are more representative of its behaviour, incorporating more comprehensive strain energy formulations. One example is the Holzapfel-Ogden model [18, 36].

Regarding the infarcted tissue, it has been assigned a linear elastic material, whereas a more appropriate approach would involve the same model used for healthy tissue adjusting the parameters to account for its higher stiffness.

Similarly, the patch has been modelled using a linear elastic material, although this choice does not faithfully represent the behavior of the polymers used to manufacture it.

For simplicity, the boundary conditions have constrained the displacements of the aortic and mitral valves in all three directions, even though they exhibit slight movement throughout the cardiac cycle. To accurately incorporate this displacement in the simulations, it would be necessary to determine its magnitude. This measurement could be obtained having CT images of the heart available throughout the entire duration of a heartbeat.

The research presented in this thesis focused on a single material and a specific auxetic geometry, utilizing a defined dimension for the patch. Consequently, to obtain a more comprehensive understanding of its behavior, it is necessary to explore alternative geometries, materials, and variations in size.

Moreover, the positioning of the device can also be subjected to change, considering that the location of the infarcted area is dependent on the specific pathological condition.

To achieve a comprehensive analysis of the phenomenon, a multiphysics simulation is necessary, taking into account both the mechanical stresses applied to the ventricle and the propagation of the action potential. The objective is to ascertain that the conductivity remains unaffected by the deformations experienced by the patch.

It’s worth noting that this study represents a preliminary phase in the pursuit of developing a patch with therapeutic properties. Therefore, it does not allow to conduct a cost-benefit analysis at this stage. However, it lays the groundwork for future and more extensive research on the subject.

Ringraziamenti

A conclusione di questo lavoro di tesi, vorremmo ringraziare il Prof. Stefano Foletti e il Prof. Jose Matas per averci dato la possibilità di raggiungere questo traguardo. Ringraziamo Ludovica Cestariolo, per la sua costante supervisione, puntualità e precisione. Un ringraziamento speciale a Matteo Gavazzoni, per averci aiutato nei numerosi momenti di dubbio. Grazie a Francesca Berti per la sua disponibilità e i suoi preziosi consigli.

Milano, Ottobre 2023

List of Figures

1.1 Heart morphology 1
1.2 Schematic representation of the ventricular musculature layers 3
1.3 Heart conduction system 4
1.4 Action potential of cardiac cells 8
1.5 Representation of the refractory states of the cardiac cells . 10
1.6 Re-entrant structures 16
1.7 Rotating unit structures 17
1.8 Chiral structures 17

2.1 Starting cell of the optimization code with a random density distribution and a uniform mesh 22
2.2 Example of final density distribution in a unit cell 22
2.3 Unit cell for PANi, phytic acid and chitosan 26
2.4 Cell obtained for PANi + PGS 28
2.5 Cell obtained for polyurethane, gelatine and CNT 28
2.6 Cell obtained for PANi and PCL 29
2.7 Cell obtained for PANi + PCL + PGS 31
2.8 Cell obtained for PANi + PCL 31
2.9 Cell obtained with PANi + PCL + PGS 33
2.10 Second cell obtained with PANi + PCL + PGS 34
2.11 Cell obtained with nanocellulose + PGS + PPy 34
2.12 Cell obtained with PANi + phytic acid + chitosan 34

3.1 Comparison of the segmentation result with different thresholds in the axial view of *3D Slicer* 38
3.2 Post-processing operations to obtain the ventricle model . 39
3.3 Construction of a solid model of the ventricle 39
3.4 Mitral valve highlighted on ventricle model 41
3.5 Heart in diastole: view from base with atria removed . . . 41
3.6 Scaling of the ventricle 42

4.1 Simplified representation of heart tissue and infarct with a parallelepiped-shaped geometry 44
4.2 Simplified model of heart tissue and rectangular-shaped patch 44
4.3 Parallelepiped-shaped model of heart tissue with auxetic patch 45
4.4 Representation of the partition of the model into four layers 46
4.5 Load and boundary conditions applied to the parallelepiped-shaped model 48
4.6 Selection of the points to verify the auxeticity of Fung's model 49
4.7 Selection of two paths to evaluate deformations in the heart tissue 50
4.8 Deformation of the heart tissue in different conditions and directions 51
4.9 Maximum longitudinal strain for each layer evaluated for infarcted ventricle with and without auxetic patch 52
4.10 Simplified representation of the infarcted ventricle using a hollow semi-ellipsoid 53
4.11 Hollow semi-ellipsoid with a patch that follows its curvature 53
4.12 Hollow semi-ellipsoid partitioned in four layers 54
4.13 Segmentation of one layer of the healthy tissue into 10° wide portions using *Matlab* 54
4.14 Load and boundary conditions applied to the ellipsoidal model 55
4.15 Pressurisation test on ellipsoidal model 56
4.16 Selection of two paths to evaluate deformations in the ellipsoidal model 57
4.17 Deformation of the ellipsoidal model in different conditions and directions 57
4.18 Model of left ventricle with an infarcted region and a patch 58
4.19 Boundary conditions applied to the ventricle model 59
4.20 Pressurisation test on Neo-Hookean ellipsoidal model . . . 60
4.21 Deformation of the ellipsoidal model in different conditions and directions, comparing Fung and Neo-Hookean models . 61
4.22 Pressurisation test on Neo-Hookean ventricle model 61
4.23 Local reference system in ventricle model 62
4.24 Selection of two paths to evaluate deformations in the ventricle model 62
4.25 Deformation of the ventricle model in different conditions and directions 63

5.1 Simplified model of heart tissue and patch 68

5.2 Simplified model of heart tissue and infarcted region 69
5.3 Transmembrane potential in a simplified model of the heart 70
5.4 Extracellular potential in a simplified model of the heart . 70
5.5 Selection of five nodes in the simplified model of the heart 71
5.6 Transmembrane and external potentials of the five nodes of the simplified model 72
5.7 Model of heart tissue with an infarcted region and a patch 73
5.8 Set of nodes from which the stimulus started in the ventricle model 74
5.9 Set of nodes from which the extra stimulus started in the ventricle model 74
5.10 Temporal evolution of the action potential using monodomain and bidomain 76
5.11 Propagation of transmembrane and extracellular potential in the heart 77
5.12 Selection of three nodes on heart tissue. 78
5.13 Temporal evolution of action potential in three nodes of the heart 78
5.14 Temporal evolution of potentials in two nodes of the heart and one on the patch 79
5.15 Propagation of transmembrane and extracellular potential in the heart with extrasystole 80
5.16 Temporal evolution of action potential in three nodes of the heart in presence of an extrasystole 82
5.17 Temporal evolution of potentials in two nodes of the heart and one on the patch, with an extrasystole 83
5.18 Parallelepiped-shaped model of heart tissue with auxetic patch 84
5.19 Transmembrane potential in a simplified model of the heart with an auxetic patch 85
5.20 Extracellular potential in a simplified model of the heart with an auxetic patch 85
5.21 Temporal evolution of potentials in three nodes of the heart: before and after the patch and on the patch itself 86

List of Tables

2.1 Bulk material properties of materials under consideration . 27
2.2 Applied constraints for each material 28
2.3 Homogeneous mechanical and conductive properties of each material 28
2.4 Bulk properties of materials under consideration with modified objective function 30
2.5 Applied constraints for each material with modified objective function 30
2.6 Homogeneous mechanical and conductive properties of each material with modified objective function 30
2.7 Bulk properties of materials under consideration with modified constraints 33
2.8 Modified constraints for each material 33
2.9 Homogeneous mechanical and conductive properties of each material with modified constraints 33
2.10 Properties of cell in Figure 2.8 35
2.11 Properties of cell in Figure 2.11 35

4.1 Experimentally derived material constants for Fung's model 46
4.2 Angle of fibre orientation with respect to x-direction 47
4.3 Properties of the linear elastic materials used for infarcted region and patch 47
4.4 Average size of mesh elements for the different parts of the parallelepiped-shaped model 47

5.1 Conductivity values in direction x, y and z for heart, infarct and rectangular patch 69
5.2 Parameters of the stimulus 69
5.3 Action potential characteristics for nodes B and C in the simplified model 72
5.4 Parameters of the extra stimulus 74

5.5 Action potential characteristics for two nodes 79
5.6 Action potential characteristics for two nodes in presence of extrasystole 82
5.7 Action potential characteristics for two nodes in presence of an auxetic patch 86

Bibliography

[1] Rubina Ajdary et al. “Multifunctional 3D-Printed Patches for Long Term Drug Release Therapies after Myocardial Infarction”. In: *Advanced Functional Materials* 30.34 (Aug. 2020) (cit. on p. 33).

[2] Anastasi et al. *Anatomia umana. Vol. 1.* Milano: Edi. Ermes, 2013. ISBN: 978-88-7051-348-6 (cit. on pp. 1–5).

[3] Khaled Alfakih et al. “Normal Human Left and Right Ventricular Dimensions for MRI as Assessed by Turbo Gradient Echo and Steady-State Free Precession Imaging Sequences”. In: *Journal of Magnetic Resonance Imaging* 17.3 (Mar. 2003) (cit. on pp. 41, 55).

[4] Kevin F. Augenstein et al. “Estimation of Cardiac Hyperelastic Material Properties from MRI Tissue Tagging and Diffusion Tensor Imaging”. In: *Medical Image Computing and Computer-Assisted Intervention MICCAI 2006*. Ed. by Rasmus Larsen, Mads Nielsen, and Jon Sporring. Vol. 4190. Berlin, Heidelberg: Springer Berlin Heidelberg, 2006. ISBN: 978-3-540-44707-8 978-3-540-44708-5 (cit. on pp. 45, 46).

[5] Zohya Azhar et al. “Bioengineered Cardiac Patch Scaffolds”. In: *Handbook of Tissue Engineering Scaffolds: Volume One*. Elsevier, 2019. ISBN: 978-0-08-102563-5 (cit. on p. 15).

[6] Olga Brazhkina et al. “Designing a 3D Printing Based Auxetic Cardiac Patch with hiPSC-CMs for Heart Repair”. In: *Journal of Cardiovascular Development and Disease* 8.12 (Dec. 3, 2021) (cit. on p. 18).

[7] Pathum Chandika et al. “Recent Advances in Biological Macromolecule Based Tissue-Engineered Composite Scaffolds for Cardiac Tissue Regeneration Applications”. In: *International Journal of Biological Macromolecules* 164 (Dec. 2020) (cit. on pp. 15, 18, 63).

[8] Parth Chansoria, Emma L. Etter, and Juliane Nguyen. “Regenerating Dynamic Organs Using Biomimetic Patches”. In: *Trends in Biotechnology* 40.3 (Mar. 2022) (cit. on pp. 14, 15, 21, 69, 88).

[9] Parth Chansoria et al. “Rationally Designed Anisotropic and Auxetic Hydrogel Patches for Adaptation to Dynamic Organs”. In: *Advanced Functional Materials* 32.43 (Oct. 2022) (cit. on pp. 14–16, 21, 63).

[10] Mei-Chin Chen, Yu-Chin Sun, and Yuan-Hsiang Chen. “Electrically Conductive Nanofibers with Highly Oriented Structures and Their Potential Application in Skeletal Muscle Tissue Engineering”. In: *Acta Biomaterialia* 9.3 (Mar. 2013) (cit. on p. 27).

[11] Sarah Clay et al. “Normal Range of Human Left Ventricular Volumes and Mass Using Steady State Free Precession MRI in the Radial Long Axis Orientation”. In: *Magnetic Resonance Materials in Physics, Biology and Medicine* 19.1 (Feb. 2006) (cit. on pp. 41, 42, 55).

[12] Piero Colli Franzone and Luca F. Pavarino. “A Parallel Solver for Reaction-Diffusion Systems in Computational Electrocardiology”. In: *Mathematical Models and Methods in Applied Sciences* 14.06 (June 2004) (cit. on p. 67).

[13] Fiorenzo Conti and Alexandra Battaglia-Mayer. *Fisiologia medica*. 2. ed. Milano: Edi-Ermes, 2010. ISBN: 978-88-7051-346-2 (cit. on pp. 6–8, 10).

[14] Darryl A. Dickerson. “Advancing Engineered Heart Muscle Tissue Complexity with Hydrogel Composites”. In: *Advanced Biology* 7.5 (May 2023) (cit. on pp. 15, 63, 69).

[15] Sait Dogan et al. “Prediction of Subclinical Left Ventricular Dysfunction with Strain Rate Imaging in Patients with Mild to Moderate Rheumatic Mitral Stenosis”. In: *Journal of the American Society of Echocardiography* 19.3 (Mar. 2006) (cit. on pp. 41, 55).

[16] Ramona Emig et al. “Passive Myocardial Mechanical Properties: Meaning, Measurement, Models”. In: *Biophysical Reviews* 13.5 (Oct. 2021) (cit. on pp. 43, 47).

[17] Paul W.M. Fedak, Patrick M. McCarthy, and Robert O. Bonow. “Evolving Concepts and Technologies in Mitral Valve Repair”. In: *Circulation* 117.7 (Feb. 19, 2008) (cit. on p. 41).

[18] H. Gao et al. “Parameter Estimation in a Holzapfel-Ogden Law for Healthy Myocardium”. In: *Journal of Engineering Mathematics* 95.1 (Dec. 2015) (cit. on pp. 45, 90).

[19] Fábio F. F. Garrudo et al. “Electrical Stimulation of Neural Differentiating iPSCs on Novel Coaxial Electroconductive Nanofibers”. In: *Biomaterials Science* 9.15 (2021) (cit. on pp. 30, 33, 69).

[20] Matteo Gavazzoni et al. “Multi-Physics Inverse Homogenization for the Design of Innovative Cellular Materials: Application to Thermo-Elastic Problems”. In: *Mathematical and Computational Applications* 27.1 (Feb. 15, 2022) (cit. on pp. 21, 27).

[21] Mahsa Ghovvati et al. “Recent Advances in Designing Electroconductive Biomaterials for Cardiac Tissue Engineering”. In: *Advanced Healthcare Materials* 11.13 (July 2022) (cit. on pp. 15, 18).

[22] Nowsheen Goonoo. “Tunable Biomaterials for Myocardial Tissue Regeneration: Promising New Strategies for Advanced Biointerface Control and Improved Therapeutic Outcomes”. In: *Biomaterials Science* 10.7 (2022) (cit. on pp. 15, 69).

[23] Jeffrey W. Holmes, Thomas K. Borg, and James W. Covell. “Structure and Mechanics of Healing Myocardial Infarcts”. In: *Annual Review of Biomedical Engineering* 7.1 (Aug. 15, 2005) (cit. on pp. 43, 47).

[24] *https://cormatrix.com/* (cit. on pp. 14, 88).

[25] *https://hdl.handle.net/10589/187315* (cit. on p. 40).

[26] *https://stemcardiocell.com/clinical-trials/acute-myocardial-infarction/* (cit. on pp. 14, 88).

[27] *https://www.dynaexamples.com/em/epintro* (cit. on p. 74).

[28] *https://www.dynasupport.com/manuals/ls-dyna-manuals* (cit. on p. 66).

[29] *https://www.lemaitre.com/products/cardiocel-bioscaffold-patch* (cit. on pp. 14, 88).

[30] Fatimah Ibrahim et al. “Cardiac Tissue Engineering: A Comparative Analysis on Microscaffold Patterning”. In: *Materials Today Communications* 33 (Dec. 2022) (cit. on p. 15).

[31] Negin Jalilinejad et al. “Electrically Conductive Carbon-based (Bio) nanomaterials for Cardiac Tissue Engineering”. In: *Bioengineering & Translational Medicine* 8.1 (Jan. 2023) (cit. on p. 18).

[32] Michaella Kapnisi et al. “Auxetic Cardiac Patches with Tunable Mechanical and Conductive Properties toward Treating Myocardial Infarction”. In: *Advanced Functional Materials* 28.21 (May 2018) (cit. on p. 21).

[33] Govinda Kapusetti, Namdev More, and Mounika Choppadandi. “Introduction to Ideal Characteristics and Advanced Biomedical Applications of Biomaterials”. In: *Biomedical Engineering and Its Applications in Healthcare*. Ed. by Sudip Paul. Singapore: Springer Singapore, 2019. ISBN: 9789811337048 9789811337055 (cit. on p. 17).

[34] Yujin Kim, Kuk Hui Son, and Jin Woo Lee. “Auxetic Structures for Tissue Engineering Scaffolds and Biomedical Devices”. In: *Materials* 14.22 (Nov. 12, 2021) (cit. on pp. 16, 17).

[35] S. A. Kleijn et al. “Normal Reference Values of Left Ventricular Strain Using Three-Dimensional Speckle Tracking Echocardiography: Results from a Multicentre Study”. In: *European Heart Journal - Cardiovascular Imaging* 16.4 (Apr. 1, 2015) (cit. on pp. 41, 55).

[36] David S. Li et al. “Insights into the Passive Mechanical Behavior of Left Ventricular Myocardium Using a Robust Constitutive Model Based on Full 3D Kinematics”. In: *Journal of the Mechanical Behavior of Biomedical Materials* 103 (Mar. 2020) (cit. on pp. 45, 90).

[37] Yimeng Li et al. “Conductive Biomaterials for Cardiac Repair: A Review”. In: *Acta Biomaterialia* 139 (Feb. 2022) (cit. on p. 18).

[38] Yuedan Li and Xiaozhong Qiu. “Bioelectricity-coupling Patches for Repairing Impaired Myocardium”. In: *WIREs Nanomedicine and Nanobiotechnology* 14.4 (July 2022) (cit. on p. 18).

[39] Marian Lorente et al. “Left Ventricle Morphometry in Healthy Humans. Long Axis, Contrast Enhanced CT Study.” In: *Scientific Medical Data* (Nov. 6, 2017) (cit. on pp. 41, 55).

[40] Damia Mawad et al. “A Conducting Polymer with Enhanced Electronic Stability Applied in Cardiac Models”. In: *Science Advances* 2.11 (Nov. 4, 2016) (cit. on pp. 26, 32, 33).

[41] Xuan Mei and Ke Cheng. “Recent Development in Therapeutic Cardiac Patches”. In: *Frontiers in Cardiovascular Medicine* 7 (Nov. 27, 2020) (cit. on p. 15).

[42] Sorina Mihil et al. “Quantitative Analysis of Mitral Annular Geometry and Function in Healthy Volunteers Using Transthoracic Three-Dimensional Echocardiography”. In: *Journal of the American Society of Echocardiography* 27.8 (Aug. 2014) (cit. on pp. 41, 55).

[43] Denisa Muraru et al. "Comprehensive Analysis of Left Ventricular Geometry and Function by Three-Dimensional Echocardiography in Healthy Adults". In: *Journal of the American Society of Echocardiography* 26.6 (June 2013) (cit. on pp. 41, 55).

[44] A. Nemes et al. "Left Ventricular Apical Rotation Is Associated with Mitral Annular Function in Healthy Subjects. Results from the Three-Dimensional Speckle-Tracking Echocardiographic MAGYAR-Healthy Study". In: *Physiology International* 107.1 (Mar. 2020) (cit. on pp. 41, 55).

[45] Attila Nemes et al. "Mitral Annulus Is Dilated with Preserved Function in Acromegaly Regardless of Its Activity: Insights from the Three-Dimensional Speckle-Tracking Echocardiographic MAGYAR-Path Study". In: *Revista Portuguesa de Cardiologia* 40.4 (Apr. 2021) (cit. on pp. 41, 55).

[46] Attila Nemes et al. "Normal Reference Values of Three-dimensional Speckle-tracking Echocardiography-derived Mitral Annular Dimensions and Functional Properties in Healthy Adults". In: *Journal of Clinical Ultrasound* 49.3 (Mar. 2021) (cit. on pp. 41, 55).

[47] Steven A. Niederer et al. "Verification of Cardiac Tissue Electrophysiology Simulators Using an N -Version Benchmark". In: *Philosophical Transactions of the Royal Society A: Mathematical, Physical and Engineering Sciences* 369.1954 (Nov. 13, 2011) (cit. on p. 68).

[48] Thilo Noack et al. "Dynamic Mitral Valve Geometry in Patients with Primary and Secondary Mitral Regurgitation: Implications for Mitral Valve Repair". In: *European Journal of Cardio-Thoracic Surgery* 56.5 (Nov. 1, 2019) (cit. on pp. 41, 55).

[49] Dinorath Olvera et al. "Electroconductive Melt Electrowritten Patches Matching the Mechanical Anisotropy of Human Myocardium". In: *Advanced Functional Materials* 30.44 (Oct. 2020) (cit. on p. 18).

[50] Roger E. Peverill. "Aging and the Relationships between Long-Axis Systolic and Early Diastolic Excursion, Isovolumic Relaxation Time and Left Ventricular Length-Implications for the Interpretation of Aging Effects on e'". In: *PLOS ONE* 14.1 (Jan. 7, 2019). Ed. by Tohru Fukai (cit. on pp. 41, 55).

[51] Roger E. Peverill et al. "Possible Mechanisms Underlying Aging-Related Changes in Early Diastolic Filling and Long Axis Motion-Left Ventricular Length and Blood Pressure". In: *PLOS ONE* 11.6 (June 28, 2016). Ed. by Jing Ai (cit. on pp. 41, 55).

[52] Roger E. Peverill et al. “Relationships of Global Longitudinal Strain with S‘, Long-Axis Systolic Excursion, Left Ventricular Length and Heart Rate”. In: *PLOS ONE* 15.7 (July 23, 2020). Ed. by Giuseppina Novo (cit. on pp. 41, 55).

[53] Taimoor H. Qazi et al. “Development and Characterization of Novel Electrically Conductive PANIPGS Composites for Cardiac Tissue Engineering Applications”. In: *Acta Biomaterialia* 10.6 (June 2014) (cit. on p. 27).

[54] Claudio Rugarli and Federico Calogaris Cappio. *Medicina interna sistematica*. 7. ed. Milano, Milano: Edra : Masson, 2017. ISBN: 978-88-214-3918-6 (cit. on pp. 13, 14).

[55] Nelson B. Schiller et al. “Recommendations for Quantitation of the Left Ventricle by Two-Dimensional Echocardiography”. In: *Journal of the American Society of Echocardiography* 2.5 (Sept. 1989) (cit. on pp. 41, 55).

[56] Ingela Schnittger et al. “Standardized Intracardiac Measurements of Two-Dimensional Echocardiography”. In: *Journal of the American College of Cardiology* 2.5 (Nov. 1983) (cit. on pp. 41, 55).

[57] Özden Seçkin Göbüt, Serkan Ünlü, and Gülten Taçoy. “Evaluation of Left and Right Ventricular Functions with Threedimensional Speckle Tracking in Patients with Mitral Stenosis”. In: *Echocardiography* 38.2 (Feb. 2021) (cit. on pp. 41, 55).

[58] Veronika Sedlakova, Marc Ruel, and Erik J. Suuronen. “Therapeutic Use of Bioengineered Materials for Myocardial Infarction”. In: *Nanoengineering Materials for Biomedical Uses*. Ed. by Emilio I. Alarcon and Manuel Ahumada. Cham: Springer International Publishing, 2019. ISBN: 978-3-030-31260-2 978-3-030-31261-9 (cit. on p. 15).

[59] Alena Shantsila et al. “A Comprehensive Assessment of Cardiac Structure and Function in Patients with Treated Malignant Phase Hypertension”. In: *International Journal of Cardiology* 167.1 (July 2013) (cit. on pp. 41, 55).

[60] Mengting Shi et al. “Micropatterned Conductive Elastomer Patch Based on Poly (Glycerol Sebacate)-Graphene for Cardiac Tissue Repair”. In: *Biofabrication* 14.3 (July 1, 2022) (cit. on p. 18).

[61] Matteo Solazzo et al. “The Rationale and Emergence of Electroconductive Biomaterial Scaffolds in Cardiac Tissue Engineering”. In: *APL Bioengineering* 3.4 (Dec. 1, 2019) (cit. on p. 18).

[62] Tan Suwatanaviroj et al. “Variability of Left Ventricular Volume and Ejection Fraction Measurements Using Contrast Echocardiography: The Influence of the Left Ventricular Length Measurements in a Large Cohort of Patients during Monitoring Cardiotoxic Effects of Chemotherapy”. In: *Echocardiography* 35.3 (Mar. 2018) (cit. on pp. 41, 55).

[63] K. H. W. J. Ten Tusscher and A. V. Panfilov. “Alternans and Spiral Breakup in a Human Ventricular Tissue Model”. In: *American Journal of Physiology-Heart and Circulatory Physiology* 291.3 (Sept. 2006) (cit. on p. 66).

[64] K. H. W. J. Ten Tusscher et al. “A Model for Human Ventricular Tissue”. In: *American Journal of Physiology-Heart and Circulatory Physiology* 286.4 (Apr. 2004) (cit. on p. 66).

[65] Farbod Tondnevis, Hamid Keshvari, and Jamshid Aghazadeh Mohandesi. “Fabrication, Characterization, and in Vitro Evaluation of Electrospun Polyurethane-gelatin-carbon Nanotube Scaffolds for Cardiovascular Tissue Engineering Applications”. In: 108.5 (July 2020) (cit. on p. 27).

[66] Udayakumar Veerabagu, Humberto Palza, and Franck Quero. “Review: Auxetic Polymer-Based Mechanical Metamaterials for Biomedical Applications”. In: *ACS Biomaterials Science & Engineering* 8.7 (July 11, 2022) (cit. on pp. 16, 17).

[67] Leyu Wang et al. “Injectable and Conductive Cardiac Patches Repair Infarcted Myocardium in Rats and Minipigs”. In: *Nature Biomedical Engineering* 5.10 (Sept. 30, 2021) (cit. on p. 15).

[68] Selwyn Wong et al. “Morphologic Features of the Rheumatic Mitral Regurgitant Valve by Three-Dimensional Echocardiography”. In: *American Heart Journal* 142.5 (Nov. 2001) (cit. on pp. 41, 55).

[69] Wenbo Zhang et al. “Simulation of the 3D Hyperelastic Behavior of Ventricular Myocardium Using a Finite-Element Based Neural-Network Approach”. In: *Computer Methods in Applied Mechanics and Engineering* 394 (May 2022) (cit. on p. 45).